Epitaxy, magnetic and tunnel properties of transition metal/MgO(001) heterostructures

2003 J. Phys.: Condens. Matter 15 R1123

(http://iopscience.iop.org/0953-8984/15/25/202)

INSTITUTE OF PHYSICS PUBLISHING JOURNAL OF PHYSICS: CONDENSED MATTER

J. Phys.: Condens. Matter **15** (2003) R1123–R1167 PII: S0953-8984(03)34582-5

TOPICAL REVIEW

Epitaxy, magnetic and tunnel properties of transition metal/MgO(001) heterostructures

C Martínez Boubeta, J L Costa-Krämer and A Cebollada

Instituto de Microelectrónica de Madrid—IMM (CNM-CSIC), Isaac Newton 8-PTM, 28760 Tres Cantos, Madrid, Spain

E-mail: alfonso@imm.cnm.csic.es (A Cebollada)

Received 12 December 2002
Published 13 June 2003
Online at stacks.iop.org/JPhysCM/15/R1123

Abstract

The main aspects of the fabrication and the structural and magnetic properties of epitaxial metal–insulator heterostructures are reviewed. Continuous and lithographically processed systems are discussed, with special emphasis on their crystalline nature when interpreting their physical properties. The work is placed within the scope of the previous and current activities by different groups on Fe/MgO(001), considered as a model system. The influence of deposition conditions on the epitaxy and morphology are discussed initially, correlating afterwards magnetic properties with crystalline structure. Subsequently, magnetic anisotropies and interactions are treated in both continuous and patterned film structures. Finally, the use of these fully epitaxial transition metal–insulator heterostructures for the development of magnetic tunnel junctions is described.

Contents

1. Introduction

The fabrication and study of single-crystalline magnetic heterostructures is highly relevant, allowing in many cases a detailed determination of the correlation between structural and morphological characteristics with the wide variety of magnetic phenomena that they exhibit. Many physical properties are more easily understood in the framework of structurally well defined materials as in the case of single crystals. For example, epitaxial magnetic heterostructures can help us to fully understand the physics involved in exciting phenomena such as spin-polarized tunnelling [1, 2], spin filtering [3], perpendicular magnetic anisotropy [4], domain wall resistivity [5], spin injection [6, 7] etc. All these phenomena can often find a direct comparison with theoretical predictions if single-crystalline structures are considered, polycrystalline or amorphous systems being more difficult to deal with. Nevertheless, the discovery and understanding of many physical properties have followed a parallel route for single-crystal and polycrystalline structures, as in the case of the giant magneto-resistance (GMR) in systems exhibiting oscillatory magnetic coupling [8–10].

From the technological point of view, most of the new phenomena exhibited in artificial magnetic heterostructures find applications in fields with a strong impact in many aspects of life. This is especially the case for magnetic storage and handling of information (including media [11], read and write heads [12] or magnetic random access memories (MRAMs) [13]), but also for the development of a wide variety of magnetic sensors used for example in the automotive industry [14]. As a matter of fact, the use of the electron's spin character in a wide variety of electronic devices is becoming so common that it has given rise to the appearance of new disciplines such as the so-called magneto-electronics or spintronics [15, 16], terms that are nowadays widely used by a large part of the scientific community.

Despite the uncontested relevance from the basic point of view, the use of high quality epitaxial magnetic heterostructures in the fabrication of commercial devices is not straightforward, the reason being that industry prefers inexpensive and easy to fabricate methods and process systems. These requirements are not always compatible with the fabrication of epitaxial heterostructures, which are often obtained in expensive molecular beam epitaxy (MBE) equipment and require the use of single-crystalline substrates. This feature is slowly changing and epitaxy requirements are no longer an impediment since nowadays epitaxial heterostructures can also be obtained by deposition techniques more transferable to industry, such as sputter deposition [17]. In addition, the increasing use of single-crystal substrates leads to their cost reduction in the market.

Crystalline order is a simplifying factor to understand and determine the physical properties of a material system. Another important characteristic to be taken into account is dimensionality. Bulk properties of a three-dimensional (3D) material can be modified by spatial boundaries, giving rise to confinement effects in two, one and zero dimensions (quantum wells, wires and dots respectively). Practical examples of the effects of dimensionality reduction are quantum well effects, first observed in semiconductor heterostructures [18]. These are also

manifested in magnetic systems such as 2D Co/Cu(001) [19], playing a relevant role in the oscillatory magnetic coupling found in this and other ferromagnetic/paramagnetic metallic heterostructures. Another example where the reduction of dimensionality determines the appearance of new phenomena is the quantum tunnelling of magnetization, where a thermally forbidden magnetization reversal is observed only in sufficiently small magnetic particles [20]. Besides dimensionality reduction effects, novel properties can be obtained by fabricating systems with sizes of the order of the characteristic length of a specific physical property. These are the so-called mesoscopic systems. In the case of magnetic materials, the relevant lengths can be the exchange–correlation length or the domain wall width when considering domain structure or magnetic interactions, or the mean free path or spin diffusion length when considering transport and magneto-transport properties.

Another recent and active research field where the spatial dimensions of the system play a relevant role is the fabrication and study of ordered arrays of nanomagnets [21]. In this case, both the reduced dimension of the magnets and their ordered arrangement can give rise to a wide variety of novel properties with potential applications. Different lithographic plus etching or lift-off techniques can be used to define the array of nanomagnets, but focused ion beam techniques have also recently been proposed for the patterning of magnetic thin films, reaching areal densities as high as $\sim$200 Gbit inch^{-2} [22]. The dimension of the magnetic entities is increasingly being reduced as well in the fabrication of MRAMs, where fundamental studies on lateral and vertical interactions between magnetic electrodes are also pertinent.

Regarding this last subject, MRAMs are basically magnetic tunnel junctions (MTJs) fabricated from metal–insulator heterostructures. Since the early work of Jullière [23], spin-dependent tunnelling between ferromagnetic electrodes across an insulating oxide [24, 25] or semiconducting [26] barriers have triggered great scientific and commercial interest. An external magnetic field in these systems modifies the electrical resistance. This changes when the magnetizations of the magnetic layers at either side of the barrier switch from antiparallel to parallel alignment. As compared with conventional memories based on semiconductor micro-fabrication [13], MRAMs present two main advantages. Firstly, there is no need of a battery to continuously refresh the state of the memory, i.e., keep a charged capacitor, and secondly, the reading process is non-destructive; i.e., to read a conventional memory the capacitor has to be discharged. This is not the case for MTJs. In this case the two states (call them 0 and 1) are an antiparallel—high resistance—and a parallel—low resistance—alignment of the electrodes' magnetization, and can be read as the tunnel junction resistance without modifying the electrodes' magnetic state. The magnetic state of the junction is changed by the field created by a current circulating through two close leads, such that the generated magnetic field is enough to switch the free layer.

From the fundamental point of view, many recent theories addressing TMR have been performed considering an epitaxial structure. The Fe/MgO/Fe(001) system has been the most commonly studied because of its simplicity. Obviously, the experimental research on magnetic tunnel structures of this composition is highly attractive.

Within this global framework, we review here different aspects of the growth and magnetic properties of continuous and tiled metal–insulator heterostructures, with special emphasis on the Fe/MgO system. In section 2 the epitaxy of ultrathin films and multilayered Fe/MgO heterostructures is described. Section 3 deals with magnetic properties such as anisotropies, magnetization reversal and magnetic interactions of the structures described in section 2. In section 4 the same issues are covered for electron beam lithography defined arrays of epitaxial (001) oriented Fe/MgO and Fe/MgO/Fe tiles. Section 5 treats transport and magneto-transport properties of these metal–insulator heterostructures. Finally, we highlight the main points in section 6.

2. Growth and structure of epitaxial Fe/MgO/Fe

Despite the great number of works describing different aspects of epitaxial metallic magnetic heterostructures (see for example [27–30]) much less work has been performed in systems like multilayered heterostructures formed by both transition metals and insulators. Insulating substrates have been widely used in the fabrication of ultrathin films and superlattices. However, insulators are seldom used as the constituent counterparts in epitaxial magnetic superlattices. In this section we review the state of the art of epitaxy and structure of transition metal–insulator heterostructures. Our main focus is the Fe/MgO system, chosen throughout as a model system.

2.1. Fe on MgO(001) epitaxy

The first reports about the epitaxial growth of bcc Fe on MgO(001) are credited to Kanaji *et al* [31–33]. They studied the behaviour of impurity atoms and adsorbed oxygen on the Fe surface and identified the Fe(001)[110] ‖ MgO(001)[100] epitaxial relation, due to a good lattice match of MgO ($a = 4.213$ Å) and Fe ($a = 2.866$ Å) upon a 45° in-plane rotation. Layer by layer growth with the formation of an epitaxial Fe film at room temperature (RT) was concluded. Low energy electron diffraction (LEED) I–V curves and the comparison with simulations allowed the determination that Fe grows pseudomorphically, with iron atoms placed above the oxygen ions. This is illustrated in figure 1, where the MgO and Fe lattices are shown, together with a cross section showing the Fe adsorption sites. In addition, LEED I–V measurements conclude a body-centred tetragonal (bct) structure at early growth stages, changing later to a bcc structure at about 10 Å average thickness.

These first results, together with the theoretical predictions by Li and Freeman [34] on the extremely low Fe–MgO interaction at the interface and the giant magnetic moment predicted for a monolayer of Fe adsorbed on MgO(001), constituted a promising starting point for the fabrication and study of Fe/MgO ultrathin films. In fact, soon after the predictions by Li and Freeman, Liu *et al* [35] produced experimental confirmation. They found a simultaneous multilayer growth in which the Fe grew with a series of terraces of different height, leading to the absence of ferromagnetic hysteresis at RT for Fe dosages below 4 monolayers, and no giant in-plane ferromagnetic moments. Unfortunately, the impossibility to obtain a real layer by layer growth at atomic level precluded the experimental confirmation of the theoretical predictions.

Obviously, it is very important to confirm theoretical calculations on ideal two-dimensional (2D) systems. For this, the fabrication of a film which is one atom thick is needed. This should cover lateral extensions large enough to be comparable with the simulated structure. Attending to thermodynamic considerations, complete wetting should be achieved whenever the sum of Fe–MgO interface and Fe surface energies is smaller than the MgO surface energy. Values of these two last quantities reported in the literature are 2.9 and 1.1 J m^{-2} respectively [36–38], but to our knowledge the Fe–MgO interface energy has not been determined. Ignoring this undetermined interface energy, Fe in principle should not wet a MgO surface, since it has a much higher surface energy. Nevertheless, standard deposition conditions correspond to a far from equilibrium situation, where conventional thermodynamic considerations do not necessarily apply. Surface diffusion then becomes a key factor in determining material transport and therefore growth modes. This is governed by the so-called Ehrlich–Schwoebel energetic barrier [39–42] encountered by an adatom upon descending a step. Thürmer *et al* [43] have found this barrier to be responsible for the pyramid-like surface aspect for the Fe/MgO(001) system in a narrow range of deposition temperatures (400–450 K).

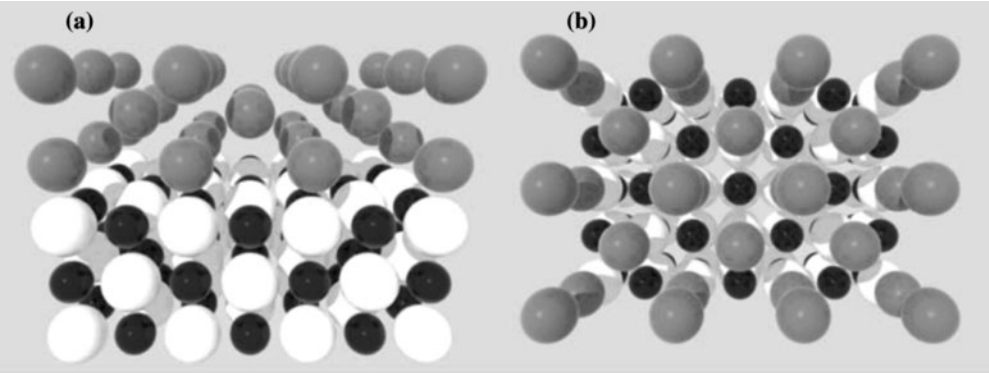

Figure 1. Sketch of the atomic positions for the Fe/MgO(001) system. Small dark spheres symbolize Mg atoms, white ones indicate oxygen atoms and grey medium spheres represent Fe atoms. (a) Side view of the Fe/MgO interface. (b) Planar view where the (001) axis is normal to the page.

At lower temperatures Fe grows forming rounded mounds, which morphology does not reflect the fourfold symmetry of the still epitaxial films. In contrast, at temperatures greater than 500 K the adatoms have enough energy to overcome the Ehrlich–Schwoebel barrier, thus giving rise to atomically flat terraces over several hundred nanometres.

Grazing incidence x-ray scattering experiments performed *in situ* by Lairson *et al* [44] confirmed the island growth mode of the first stages of the Fe/MgO(001) epitaxy by sputtering. They found an increase in the Fe lattice parameter for increasing thicknesses in the 1–10 monolayer regime, relaxing back to bulk values for higher coverages. Agglomeration of islands into a continuous film at about 20 monolayers is accompanied by changes in the Fe lattice parameter and high-angle diffraction peak widths, probably due to the accompanying strain relaxation.

The fact that the temperature ranges for 2D versus 3D Fe growth do not coincide for different experimental groups can be due, among other reasons, to the different deposition techniques used. While the impinging atoms in thermal evaporation have energies of the order of tenths of electron volts, the sputtering technique is characterized by a particle energy distribution that has a maximum around 5–10 eV, presenting as well a high energy tail with a low percentage of sputtered particles that can reach up to several hundred electron volts of energy. These energetic particles have been attributed as the origin of a high density of nucleation centres. They can modify growth kinetics with respect to thermal evaporation deposition [45], as they can originate a high density of nucleation centres by their impact on the sample surface. Another possible source of the difference between both deposition techniques would be the increase in the effective surface temperature during growth induced by these energetic particles [46].

Until now only a few examples of the epitaxial growth of Fe on bulk MgO(001) single crystals have been presented. Nevertheless, the epitaxial growth capability of MgO(001) thin films on GaAs(001) allows the extension of previous studies on the Fe/MgO(001) system to high quality and technologically relevant substrates. It has been demonstrated that it is possible to grow high quality epitaxial Fe(001) thin films on MgO buffered GaAs(001) substrates, showing a strong dependence of the Fe morphology on the deposition temperature [47, 48]. These structures are grown by a combined use of triode sputtering and laser ablation in a UHV deposition system. Epitaxial MgO buffer layers, 100 Å thick, were grown at 450 °C by laser

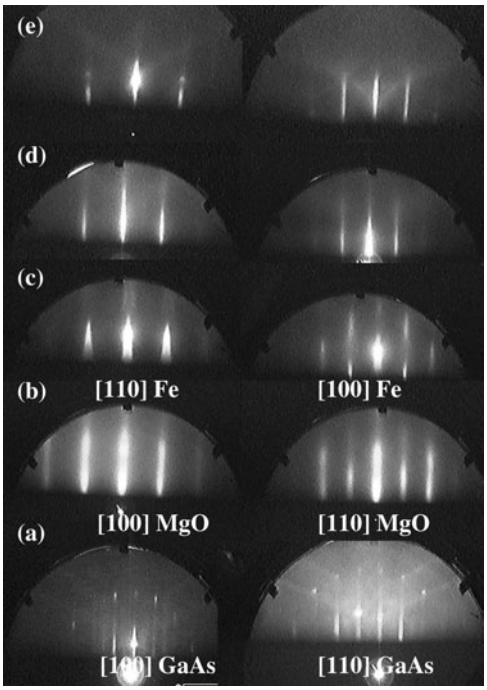

Figure 2. RHEED patterns at different stages (a)–(e) during the deposition of an Fe/MgO heterostructure on GaAs(001); see text for details. Reprinted from [48] ©2001, with permission from Elsevier.

ablation on clean GaAs surfaces after desorption of an As_2 protective layer. Thin Fe films were subsequently deposited by triode sputtering at different growth temperatures on the MgO buffer layers. Figure 2 presents reflection high energy electron diffraction (RHEED) patterns of the subsequent steps in the cleaning of GaAs, deposition of MgO buffer layer and deposition of Fe films on top of the MgO. Diffraction patterns are shown for two different azimuths, which allows simultaneous determination of the epitaxial relation between different films. In figure 2(a) the RHEED pattern for the clean GaAs(001) after As desorption is shown, with characteristic narrow and intense streaks as well as Kikuchi lines. The diffraction pattern after deposition of a 100 Å MgO(001) thin film is shown in figure 2(b), with broader but very intense and well defined streaks. Epitaxial Fe(001) films grown on this MgO layer are obtained by sputter deposition at RT as presented in figure 2(c). The obtained epitaxial relations are the expected Fe(001)[110] ‖ MgO(001)[100] ‖ GaAs(001)[100]. Notice the faceted structure of the Fe surface, as revealed by the chevron shape of the diffraction streaks. This faceting disappears after a mild annealing at 400 °C for 15 min (figure 2(d)). Increasing the Fe deposition temperature up to 500 °C instead of RT onto the MgO(001) surface gives rise to very flat surfaces as evidenced by the high quality RHEED patterns shown in figure 2(e). Oka *et al* [49] have demonstrated that for annealed Fe thin films epitaxially grown on polished MgO(001) substrates, a $c(2 \times 2)$ RHEED reconstruction appeared as indicative of a step-terrace-based thin film surface that was atomically flat and with no impurities. The $c(2 \times 2)$ reconstructed surface never occurred at annealing temperatures below 493 K, and the critical thickness at which the observed diffraction patterns changed from (1×1) into $c(2 \times 2)$ depend on the annealing temperatures; with increasing annealing temperatures, the critical thickness is decreased. We have observed the presence of this reconstruction in some, but not all, of the films grown at intermediate and elevated

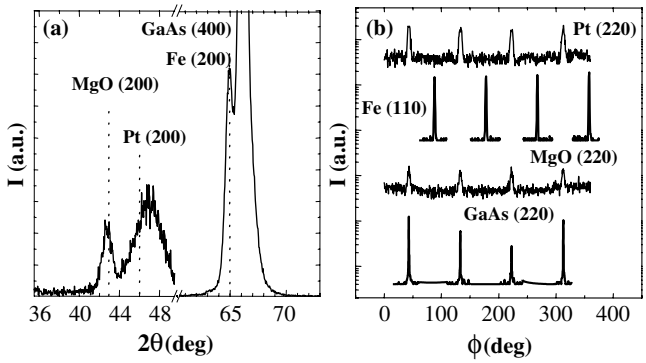

Figure 3. XRD characterization of a Pt/Fe/MgO/GaAs(001) heterostructure. (a) Symmetric scans (vertical dotted lines indicate bulk positions for MgO, Pt and Fe(200) reflections). (b) Asymmetric ϕ-scans. Reprinted from [48] ©2001, with permission from Elsevier.

temperatures. Since this is a non-systematic finding, it is possible that residual contamination during or after the sputter deposition of Fe was responsible for this absence of reconstruction.

Further structural characterization of these films can be performed *ex situ* by x-ray diffraction (XRD). In figure 3 we show a compilation of symmetric and asymmetric XRD scans for a 25 Å Pt/200 Å Fe/100 Å MgO/GaAs(001) structure. In the high angle $2\theta/\omega$ scan (figure 3(a)), four peaks are clearly observed, corresponding to the substrate, Fe film, Pt capping and MgO buffer layers. The Fe(200) appears very close to the GaAs(400) reflection, whereas MgO and Pt(200) peaks are shifted with respect to the bulk value, indicating the presence of a growth induced residual strain. Remarkably, the peak of the thin capping layer, only 25 Å thick, is clearly observed, which demonstrates the high crystalline quality of the whole structure. The crystalline coherence lengths extracted from the Fe(200) peak widths are around 100 for 200 Å thick deposits, while mosaic spreads are typically 1°. In figure 3(b) ϕ scans for asymmetric reflections of substrate and the three layers are shown, as additional verification of the already mentioned epitaxial relations.

The influence of the deposition temperature on the Fe morphology can be further studied by atomic force microscopy (AFM). Figure 4 shows images for Pt capped Fe films grown at different temperatures onto MgO/GaAs(001) substrates together with the corresponding RHEED patterns for two different azimuths. Deposition of Fe at RT and up to 200 °C yields very flat surfaces. These are featureless as observed *ex situ* by AFM characterization, as shown in figure 4(a). Nevertheless, it cannot totally exclude the presence of morphological elements, specially holes, of nanometric and subnanometric dimensions that would not be observable by this technique due to the convolution with the tip shape. Clear morphological features become evident as the Fe deposition temperature is increased. A uniform distribution of holes is clearly observed in the surface of the film grown at 300 °C (not shown), reflecting the non-wetting characteristics of the Fe on MgO under these specific deposition conditions. The effect of deposition temperature on the film morphology becomes more evident for the sample grown at 400 °C (figure 4(b)). At this temperature the film starts to exhibit a dendritic character, with rounded areas that fill the substrate surface but that are separated by unfilled regions. All these rounded regions are nevertheless in physical contact. For Fe deposited at 500 °C, a clear 3D growth is already observed, with islands of non-defined shapes that do not coalesce and are separated from each other. This effect is even stronger for deposition at 700 °C (figure 4(c)), where island growth mode is more pronounced, and the islands exhibit geometrical square and rectangular shapes due to their crystalline nature and match with the substrate. Let us recall

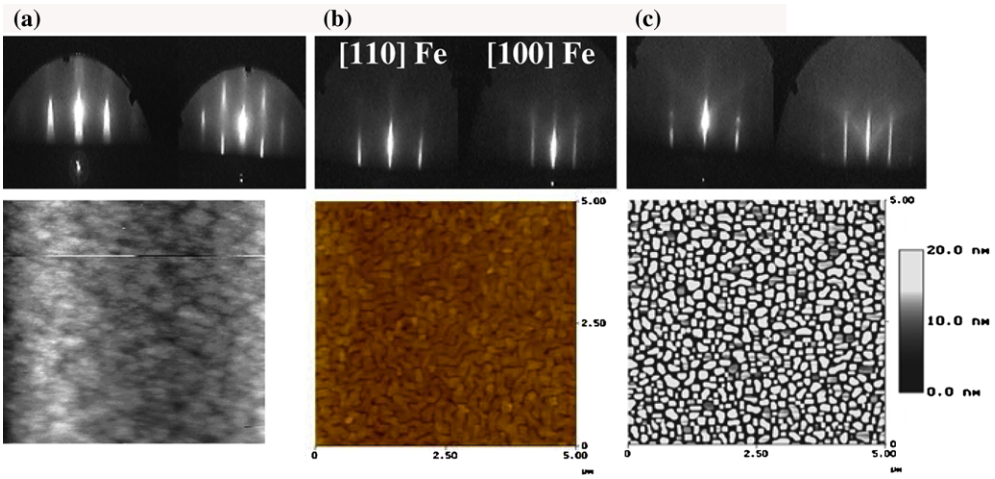

Figure 4. AFM images ($5 \times 5\ \mu m^2$ scans) showing the morphology of Pt/Fe/MgO/GaAs(001) thin films grown at (a) RT, (b) 400 and (c) 700 °C. RHEED patterns for the corresponding Fe layer are also shown.

(This figure is in colour only in the electronic version)

at this point that in all cases the islands are crystalline and with epitaxial registry with respect to the MgO(001) underneath, as shown by RHEED measurements. As a matter of fact, both crystalline quality and surface flatness of the individual islands increases as the deposition temperature increases. This change in morphology as a function of the deposition temperature is a clear example of the influence that kinetic parameters have on the final morphology in thin film deposition, and how, as the system temperature is increased, the Fe atoms have enough energy to surface-diffuse, overcoming surface and step edge barriers and allowing the system to find the actual thermodynamic equilibrium situation. On the other hand, this example shows the necessity of using both reciprocal space as well as real space characterization techniques to fully identify the structural nature of a system. Note for example that just by analysing the RHEED pattern of the sample grown at 700 °C, one could easily conclude the presence of high quality, flat and continuous films, while AFM measurements demonstrate that this flatness only extends over areas of the order of the RHEED electrons' coherence length.

The reader is referred to [50–59] for further detailed aspects related to the epitaxy, morphology and structure of Fe/MgO(001).

2.2. Epitaxial Fe/MgO/Fe trilayers

A large number of studies have been devoted to the growth of Fe on MgO, in contrast with far fewer reports treating the epitaxy of MgO on Fe(001), despite the fact that the epitaxy of oxides on metals is a very interesting field, as reflected in recent reviews [60, 61]. This trend has changed, and now more groups have been able to obtain epitaxial Fe/MgO/Fe multilayered structures. Previous works dealing with systems very similar to those treated in this review are the epitaxial growth of MgO on V(001) and Nb(001) [62], Mo(001) [63–66], Cr_xMo_{1-x} [67] and Ag(001) [68–71]. The interest in growing epitaxial insulator on metallic surfaces has followed different basic and technological motivations. Among these, specially interesting are the results reported in [71] on the MgO epitaxy on Ag(001), with outstanding insulating properties of MgO ultrathin films, such as a 6 eV bandgap formed for three MgO monolayers grown on Ag(001).

As already mentioned, published works on the epitaxy of MgO on Fe(001) are scarce. The first reported study by Park *et al* [72] was initially motivated by the use of MgO as a substrate, with capping layers that electrically isolated atom thick Fe films. This was analysed contrasting theoretical predictions for free-standing ferromagnetic monolayers [34]. Deposition by electron beam on Fe(001) buffer layers at 700 K produced flat and epitaxial MgO films for a thickness as low as 5 Å, with an improvement of crystalline quality as the thickness increased. The large difference in surface free energies, much lower for MgO than for Fe, was the main ingredient to explain the 2D growth. As expected from symmetry considerations and the growth of Fe on MgO, the observed epitaxial relation was MgO(001)[100] ∥ Fe(001)[110]. It is worthwhile to mention subsequent works of Vassent *et al* [73, 74], studying by diffraction techniques the strain relaxation and the surface deformation of thin MgO films deposited on Fe(001). However, in these studies, the use of MgO as tunnel barrier was not considered. This was done by Keavney *et al* [75] with the fabrication of an Fe/MgO/Fe epitaxial trilayer. In these structures ferromagnetic coupling was found between both Fe layers for MgO thicknesses below 75 Å, due to the presence of pinholes that were observed by SEM.

Nowadays, several groups have focused their work on the magneto-transport properties of tunnel junction structures, and have reported the fabrication of high quality epitaxial Fe/MgO/Fe multilayered heterostructures, either on semiconductor substrates [48, 76–79], polished Fe(001) single crystals or whiskers [80, 81] on MgO(001) bulk surfaces [82–84]. In all cases, the use of high quality flat substrates and an accurate control of the deposition conditions are compulsory requirements to obtain epitaxial heterostructures with sharp interfaces and very little or no conformal roughness. This is illustrated for the case of growth on GaAs(001) single crystals at different temperatures. In figure 5 we show a transmission electron microscopy (TEM) image of a multilayered Fe/MgO epitaxial heterostructure grown on GaAs of high structural quality. RHEED patterns taken at the different stages of the deposition of the layers demonstrate how the epitaxial character is maintained along the different stacks. To obtain this kind of structure, the deposition temperature of the MgO was maintained at 400 °C, whereas Fe was grown at RT (to avoid excessive surface diffusion and the consequent 3D growth) and then annealed at 400 °C to flatten out the faceted Fe surface. As shown before, the deposition of Fe on MgO at 400 °C produces epitaxial high crystalline quality Fe. But Fe grows in islands, seriously affecting the structure of the Fe/MgO multilayer morphology if completely grown at this temperature. This is shown in the TEM image in figure 6 together with the RHEED patterns at different layer growth stages.

2.3. The nature of the Fe–MgO interface

A very important factor determining the physical properties of ultrathin layers and multilayered heterostructures is the structure of the interface, either with the substrate, other layers or vacuum. Symmetry breaking, intermixing or hybridization effects can modify and even give rise to new physical properties, a clear example of which is the magnetic anisotropy in metallic multilayers [85]. Another field where the interface structure plays a relevant role is in the determination of the transport and magneto-transport properties of tunnel junctions. Both properties are directly related to the density of states of top and bottom electrodes at the interface with the oxide tunnel barrier [86].

As mentioned before, ten years ago MgO appeared as a good candidate for a substrate and capping layer for a system able to confirm theoretical predictions for the properties of a free standing Fe atomic layer. This was mainly due to a modest charge transfer theoretically calculated for Fe and Ag on MgO(001) at the interface [34, 87]. It is well accepted that Fe and Ag atoms sit above the O sites on a clean MgO(001) surface. It has also been widely

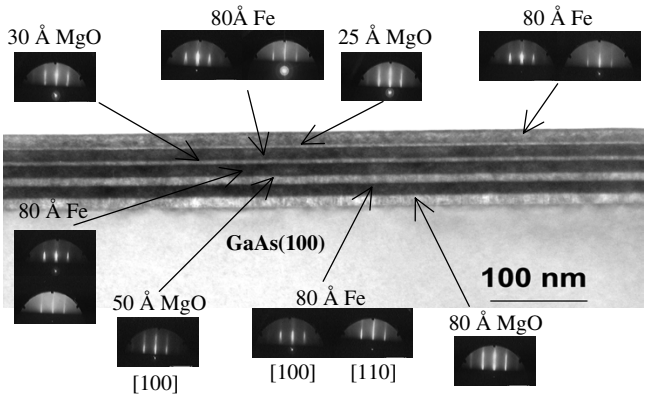

Figure 5. TEM image of an Fe/MgO multilayered structure grown on GaAs(001). MgO layers were grown at 400 °C; Fe layers were grown at RT and annealed at 400 °C for 15 min. The Fe thickness is kept equal to 80 Å for all the layers, whereas the MgO layer thicknesses are (bottom to top) 80, 50, 30 and 20 Å. RHEED images acquired during the different steps of the growth are shown.

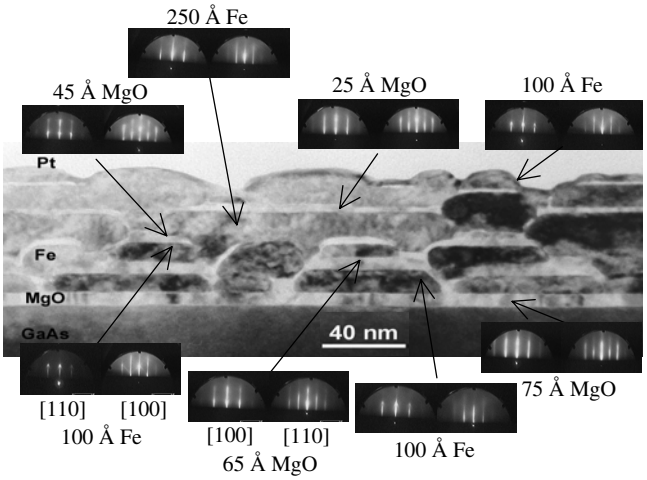

Figure 6. TEM image for a Fe/MgO multilayered structure grown on GaAs(001). Both MgO and Fe layers were grown at 400 °C. Thicknesses for the subsequent Fe and MgO deposits (bottom to top) are 100, 100, 250 and 100 Å and 75, 65, 45 and 25 Å respectively. RHEED images acquired during the different steps of the growth are also shown.

accepted that the metal–O bond is more significant than the metal–Mg bond. Nevertheless, Tanaka *et al* [88] have obtained by first-principles calculations that the metal–Mg covalent bond predominantly determines the interfacial bond strength. These results suggest, the charge transfer across the metal–MgO interface being very small, that even when the metal atoms are located on top of O atoms, those cannot be oxidized, since the formal charge of these O atoms on the surface is already -2.

It is clearly desirable to test these theoretical calculations with experiments. This is possible for the case of the Fe/MgO system, in view of recent results by Meyerheim *et al* [89, 90], where they present the geometrical and compositional structure at the interface of MgO deposited on Fe(001) substrates. Using surface XRD, they conclude the existence of a

substoichiometric FeO interface layer between the substrate and the MgO film. This can affect the tunnel transport across the interfaces in a Fe/MgO/Fe heterostructure. An open question is the nature of the symmetric Fe on MgO(001) interface, which is nominally equivalent, but that in real systems might exhibit different properties. For example in Fe/MgO/Fe and FeCo/MgO/Fe tunnel junctions exhibiting tunnel magneto-resistance [76, 82] the MgO/Fe interface is formed during MgO deposition at elevated temperatures with the very likely presence of atomic O which favours the oxidation of the Fe(001) surface. On the other hand, the Fe/MgO and FeCo/MgO interfaces are formed during the top electrode deposition at RT on a well formed, stable MgO(001) surface, and therefore both interfaces might be different.

Since deposition conditions, fabrication techniques and even the sequence of deposition (either Fe on MgO or MgO on Fe) can determine the specific nature of the Fe/MgO interface, an in-depth structural and chemical characterization must be carried out for each specific system in order to ascertain the exact nature of the interface.

3. Magnetic properties of continuous Fe/MgO/Fe heterostructures

The magnetic properties of the structurally characterized Fe/MgO and Fe/MgO/Fe sytems are described in what follows following a similar scheme. This is another instance of fundamental phenomena where first-principles theories that quantitatively explain the experimental situation are required.

Magnetic anisotropy of ultrathin films is being exploited for the development of new magnetic devices and sensors. It is mainly determined by the underlying anisotropies in the film's atomic structure, including magneto-crystalline anisotropy distorted by chemical ordering and alloying, magneto-elastic anisotropies through the presence of strain due to epitaxy and to formation of defects, and extrinsic characteristics such as the system size and morphology. On the other hand, magneto-static energy and dipolar interactions play a fundamental role in the reversal mechanism of patterned structures and nano-elements. The following sections include detailed discussions of these phenomena.

3.1. Fe on MgO(001): magnetic properties and magnetization reversal in continuous single layers

In bulk form, bcc Fe has a magnetic moment of $2.2\,\mu_B$ and exhibits a cubic magnetic anisotropy with an anisotropy constant K_1 of 4.8×10^5 ergs cm^{-3}, the $\langle 100 \rangle$ directions being the easy magnetization axes. One of the motivations of growing metal ultrathin films is to obtain phases that exhibit properties different from those of bulk. This was the case with the theoretical predictions by Li and Freeman [34] on the giant magnetic moments obtained for a monolayer of Fe on MgO(001). Their calculations yielded values of $3.07\,\mu_B$, very close to the $3.10\,\mu_B$ obtained for a free standing Fe layer [91]. This was attributed to the lack of electronic interaction between Fe and MgO ($<$0.05 e/atom of charge transfer at the interface) and therefore the very unlikely chemical interaction. The increase in the magnetic moment was even predicted for the case of two monolayers of Fe on MgO(001), which would present $2.96\,\mu_B$ at the surface and $2.85\,\mu_B$ at the interface. These are similar values to those predicted for one atomic layer of Fe on Au(001) ($2.97\,\mu_B$) and for the surface of Fe in bcc Fe(001) ($2.98\,\mu_B$) [92–94]. A first set of experiments pursuing the corroboration of these predictions were performed by Liu *et al* [35] using surface magneto-optic Kerr effect (SMOKE) and Huang *et al* [95] using SMOKE and neutron diffraction techniques. Liu observed the absence of ferromagnetic hysteresis for thicknesses below 4 monolayers, probably due to the simultaneous multilayer growth mode that provided a superparamagnetic character to the Fe patches. No giant magnetic moment

was found in Huang's experiments with bulk values for the magnetic moment of all the Fe films studied, regardless of the thickness of the film. Again the film morphology, far from an ideally planar structure considered in theoretical calculations, played a very important role in determining the physical properties of the experimentally studied structures. It is worth mentioning that, to date, there has not been any clear experimental corroboration of a giant magnetic moment in the Fe/MgO(001) system.

Another physical property that has been a topic of intensive study is the determination of magnetic anisotropies in these Fe(001) ultrathin films. Due to their epitaxial character, the expected in-plane cubic anisotropy has experimentally been found in the Fe/MgO(001) system, with an in-plane anisotropy and the easy axis along the ⟨100⟩ in plane directions. Early works of Goryunov *et al* [96, 97] determined the magnetic anisotropy for Fe films of different thicknesses sputtered on MgO(001) substrates. Assuming the weak electronic interaction at the Fe–MgO interface, their goal was to explore the relevance of the mismatch induced strain on the magnetic anisotropy of the system. They found an important surface anisotropy contribution up to thicknesses around 1000 Å, due to strain relaxation extended to distances as far as 45 Å from the film–substrate interface. This misfit relaxation was related to the in-plane angular dispersions of the cubic and uniaxial magnetic anisotropy axes studied by Fermin *et al* using ferromagnetic resonance [98] in thin Fe films sputtered onto MgO(001) substrates.

It has been demonstrated that the deposition geometry can be another source of additional magnetic anisotropies, specially in the oblique-incidence deposition geometry of Fe/MgO(001) [99–101]. In the first two cases, this anisotropy was due to an oriented morphology as determined by x-ray photoelectron diffraction and STM respectively. This would produce a shape like magnetic anisotropy of dipolar nature. In the second case, Durand *et al* performed an XRD characterization of their films, assigning the origin of the uniaxial anisotropy to an in-plane tetragonal Fe lattice distortion in the whole volume of the films. This gave rise to a magneto-elastic character for the uniaxial anisotropy.

The relevance of the Fe–substrate interface in the modification of the magnetic anisotropy of the whole film has been contrasted in several works. An additional in-plane uniaxial anisotropy has also been observed in Fe(001) thin films as thick as 350 monolayers grown on GaAs, InAs or even ZnSe(001) semiconductor substrates [102–106]. This anisotropy was assigned as of pure interfacial origin, being often attributed to the intrinsic anisotropy of the dangling bonds at the GaAs(001) surface. Nevertheless, the substrate surface preparation has been revealed to be crucial to obtain this anisotropy [107]. Another source of magnetic anisotropy localized at the film–substrate interface is, for example, the surface step anisotropy, being even intentionally induced by deposition on vicinal substrates (see for example [108–111]). It can even be intentionally controlled varying the step density [112].

The presence of steps in the substrate is the argument to explain the observed magnetic anisotropy found in Fe(001) thin films deposited at normal incidence on MgO(001) by sputtering, since no structural anisotropy was experimentally measured in the Fe film itself [113–115]. In figure 7 we show Kerr loops for a 200 Å Fe(001) thin film with the magnetic field applied along the main in-plane crystallographic directions. As expected, the [100] and [110] correspond to the easy and hard magnetization axes respectively (figures 7(a) and (b)). However, in figure 7(c) the hysteresis loop for the field applied along the [010] direction clearly shows plateaus at low fields which demonstrate different magnetization reversal processes than for the crystallographically equivalent [100] axis. The differences are attributed to an additional uniaxial magnetic anisotropy present in the film.

This is further evidenced by a systematic study of the longitudinal and transverse magneto-optical response of this film for different orientations of the crystalline axes with respect to

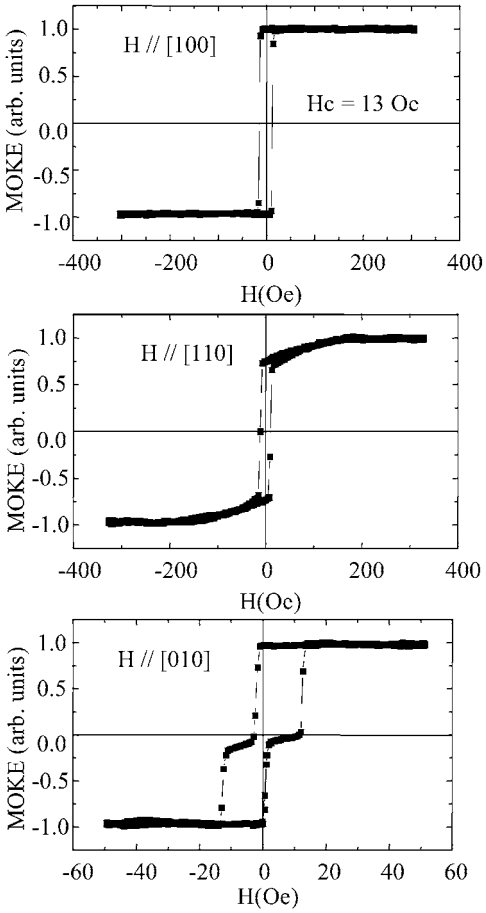

Figure 7. Kerr hysteresis loops for a 200 Å Fe(001) thin film. The magnetic field is applied along the [100], [110] and [010] directions.

the applied magnetic field. In figure 8 we show a series of these measurements for different relative angles, 0° corresponding to the [100] direction parallel to the applied magnetic field. In this case, the longitudinal signal (component parallel to the applied magnetic field) presents a typical square hysteresis loop with 100% remanence and low coercive fields, around 10–15 Oe. As sketched, the 90° orientation corresponds to the [010] crystalline direction parallel to the magnetic field. In the same case the longitudinal Kerr loop exhibits two plateaus of zero signal in the low magnetic field regimes. These plateaus are simultaneous with absolute maxima in the transverse component of the Kerr signal, which indicates that at these magnetic fields the magnetization is rotating 90° with respect to the [010] direction, therefore pointing along the [100] direction. Consequently one can conclude that an additional uniaxial anisotropy exists superimposed on the crystalline biaxial anisotropy. Domain observations by Kerr microscopy corroborate these conclusions [114]. Other relative orientations are shown in figure 8, illustrating the complex magnetization reversal behaviour for this system. Since these structures were deposited at normal incidence and no asymmetry in the strain was observed in the film plane by XRD characterization, it was concluded that the source of the additional anisotropy was of interfacial origin, and probably due to the presence of steps in the MgO substrate.

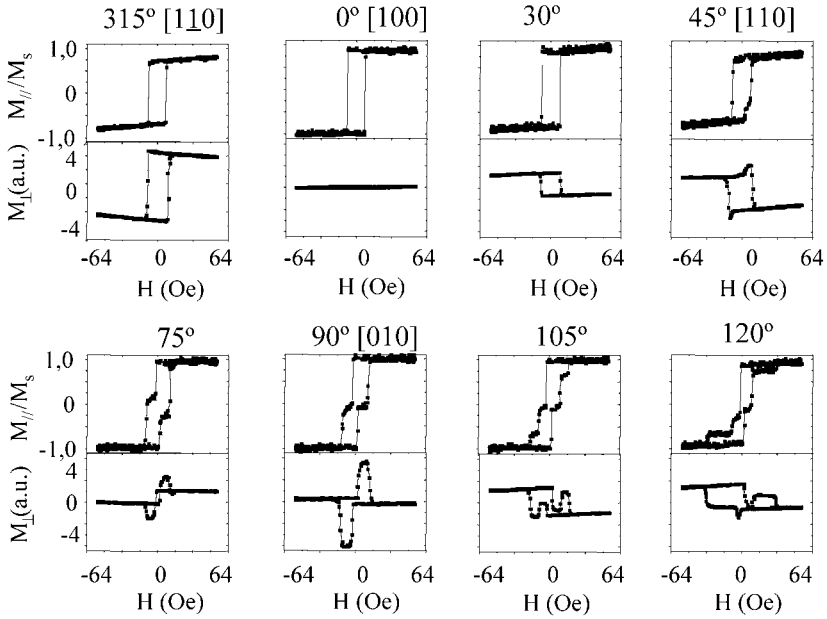

Figure 8. Transverse ($M_\perp$) and normalized to saturation longitudinal ($M_\parallel/M_s$) Kerr loops for a 200 Å Fe(001) thin film with the magnetic field applied along different in-plane directions. Reprinted from [114] ©2000, with permission from Elsevier.

A very powerful technique for the magnetic characterization of magnetic heterostructures is the transverse biased initial susceptibility (TBIS) by MOKE, which has been demonstrated to be very useful for the determination of in-plane uniaxial, biaxial and mixed anisotropies [116]. An example of the application of this technique for the study of the magnetic anisotropies in Fe films with mixed in-plane uniaxial and biaxial anisotropies is shown in figure 9. Observe susceptibility and inverse susceptibility curves for a 200 Å Fe(001) film [113, 115] whose Kerr loops were shown in figure 7. In figures 9(a)–(c) the susceptibility curves are shown for the magnetic field applied along the [100], [010] and [110] in-plane Fe directions respectively. The susceptibility response for the [100] case is typical for a magnetic field applied along a magnetic easy axis [117]. For the H ∥ Fe[010] direction (figure 9(b)), the dip observed in the susceptibility can be explained by the nucleation of domains magnetized along the [100] direction, and a magnetization reversal therefore driven by 90° walls. This is more clearly shown in the inset, allowing an accurate determination of the range of fields where the domains magnetized parallel to the [100] direction nucleate and propagate. In figure 9(c) the susceptibility exhibits again the typical shape when the magnetic field is applied along a hard axis. From these measurements, the inverse of the susceptibility can be directly calculated, as shown in figures 9(d)–(f). These allow an accurate determination of the effective anisotropy fields of the film along specific directions by performing lineal extrapolations of the high field range and determining the crossing point with the field axis.

We have previously shown that the deposition temperature strongly affects the morphology of Fe thin films grown on MgO buffered GaAs(001), obtaining continuous and flat films for RT depositions, island growth mode at 700 °C and dendritic structures at intermediate temperatures. This morphology evidently has strong consequences in the effective anisotropy and magnetization reversal processes which can be determined by a combined Kerr loops and TBIS characterization [118]. In figure 10 we show Kerr hysteresis loops for three of these

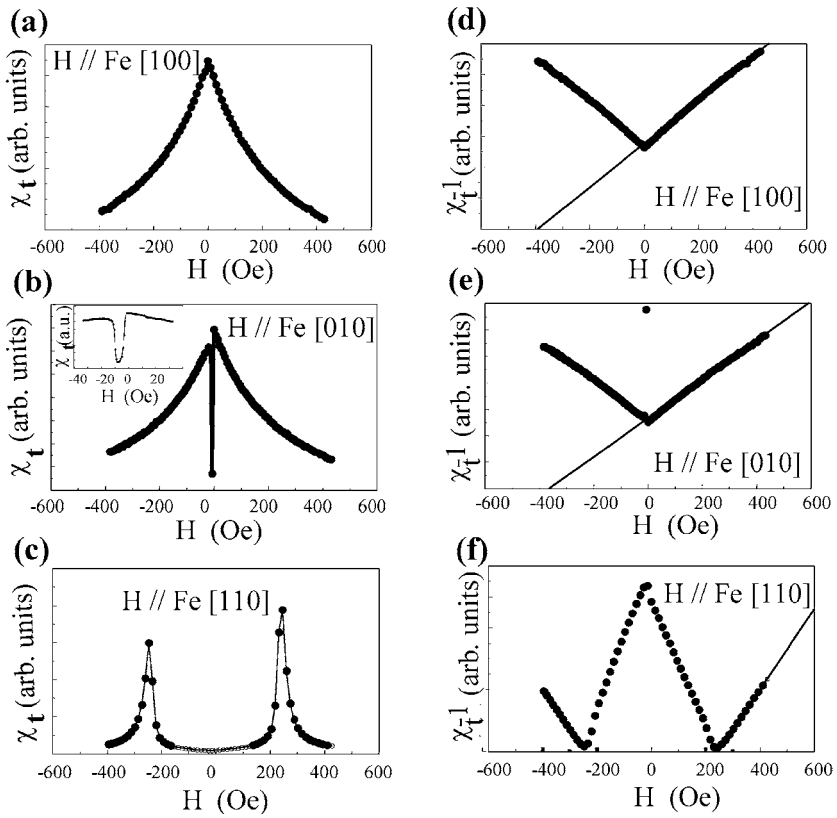

Figure 9. TBIS for a 200 Å Fe(001) thin film with the magnetic field applied along (a) [100], (b) [010] and (c) [110] directions. Panels (d)–(f) show the respective inverse susceptibility. The inset to panel (b) shows the low field region in more detail, taken from [115, 116].

samples, namely those deposited at RT, 400 and 700 °C, representative of flat, dendritic and island growth modes. The magnetic field is applied along easy [100] and hard [110] axes. The usual hysteresis loops are obtained for the RT sample (figure 10(a)), characteristic of a well defined magneto-crystalline anisotropy as discussed above. Nevertheless, this anisotropy becomes less evident as the deposition temperature increases, giving rise to a transition from a continuous and flat growth to a dendritic-like structure. Figure 10(b) shows the obtained hysteresis loops for the sample grown at 400 °C. Loops for the applied field along [100] and [110] axis are now more similar to each other, presenting a relatively high remanence-to-saturation ratio (0.9 and 0.8 respectively). The higher coercive fields obtained for this sample with respect to that grown at RT are clearly related to the morphological features present in the 400 °C sample. A simple model considering domain wall pinning at the narrow necks of the dendritic structures can reasonably reproduce the experimentally obtained values [118]. Notably, even though the film morphology is relatively symmetric and with round dendrite shapes, the magneto-crystalline anisotropy intrinsic to the structure is still evident when plotting for example the coercive field as a function of the angle between the applied field and the Fe crystalline directions, as shown in the panel at the top of figure 4(b).

At 700 °C deposition temperature, corresponding to square and rectangular island growth mode, the hysteresis loops for the applied field along [100] and [110] directions are basically equivalent, with no noticeable effect of the magneto-crystalline anisotropy still present in each

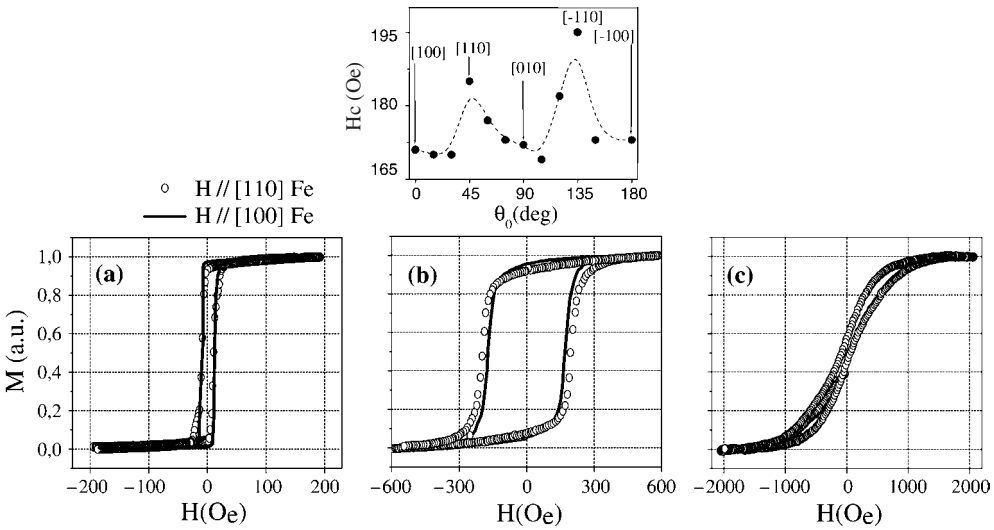

Figure 10. Kerr loops for three Fe(001) thin films grown at (a) RT, (b) 400 °C and (c) 700 °C. The panel at the top of figure 10(b) corresponds to the coercive field plotted as a function of the angle between the applied field and the Fe crystalline directions.

individual island. In figure 10(c) the hysteresis loops for this sample are now characterized by their low remanence and coercivity. This behaviour suggests the presence of strong negative demagnetizing local fields.

Thus, at the saturated state the magnetic behaviour of all the samples is governed by K_1 of single-crystalline Fe, independently of the growth temperature. Differently from this, and due to their local morphology, the magnetization properties of the sample evolve as the deposition temperature increases from a nucleation–propagation domain wall mechanism, taking place in smooth continuous films, to pinning, occurring in self-patterned films with a homogenous distribution of defects. Finally the reversal turns fully isotropic for tiled films composed of rectangular elements.

3.2. Fe/MgO/Fe: magnetic coupling in continuous trilayers

In the examples described so far we have analysed the magnetization reversal of single Fe layers. Since transport and magneto-transport properties will be treated in another section, here we restrict the discussion to studies specially related to the magnetic coupling/interaction between both ferromagnetic layers. There are basically three possible origins for this coupling:

(1) indirect exchange coupling,
(2) dipolar coupling, either due to 'orange peel' effects or to stray fields originating from domain walls of either of the layers, and
(3) direct ferromagnetic coupling through pinholes.

Several models have been proposed for the possible existence of exchange coupling between two ferromagnetic layers separated by an insulator [119–121]. First experimental results were probably due to Pomerantz *et al* [122], who studied the Fe/C/Fe system by ferromagnetic resonance and that indeed motivated Slonczewski's subsequent theoretical work. Several years later, Keavney *et al* [75] faced the study of the conductance and magnetic coupling in epitaxial Fe/MgO/Fe(001) trilayers. For this study several Fe/MgO/Fe trilayers were grown

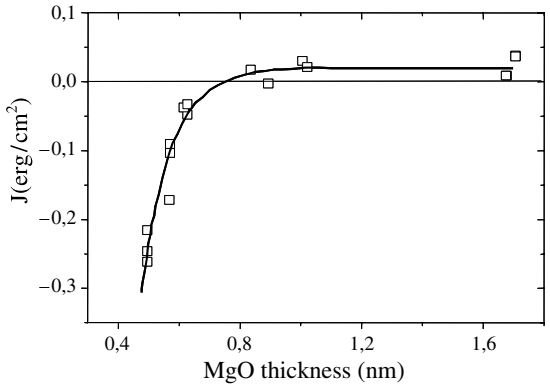

Figure 11. Variation of the coupling strength J between two Fe layers in an Fe/MgO/Fe structure with the interlayer MgO thickness, taken from [83].

with varying MgO thickness between 12 and 75 Å. The bottom Fe layer was pinned to a thick Fe layer via antiferromagnetic coupling through 9 Å of Cr. They observed by the MOKE effect a clear switching from AFM to FM orientation for both Fe layers in contact with the MgO spacer, the switching field being strongly dependent on the MgO thickness. Unfortunately, via transport measurements, no MgO spacers with thicknesses below 40 Å were found to be insulating, due to the presence of pinholes. The observed thickness dependence of the switching field was then assigned to a thickness dependence of pinhole size or pinhole density. In fact, the effect of pinholes has been revealed to be very important, obviously in the transport behaviour of tunnel junctions, but also in the magnetization reversal of multilayered heterostructures. This last effect on the hysteresis loops has been modelled for antiferromagnetically coupled (AFC) multilayers [123], giving rise to ferromagnetic, antiferromagnetic or a mixture of both states depending on pinhole size and separation.

Interlayer magnetic coupling through MgO spacers has also been studied by van der Heijden *et al* [124] who fabricated Fe_3O_4/MgO/Fe_3O_4 trilayers, again finding ferromagnetic coupling due to pinholes for MgO thicknesses below 13 Å and due to 'orange peel' coupling [125] effects above this thickness. Obviously, a tight control on the spacer quality, with absence of pinholes, is a big challenge, and it was not until very recently that Popova *et al* showed their capability to obtain continuous insulating MgO spacers as thin as 8 Å in Fe/MgO/Fe epitaxial heterostructures [82], and the observation of interlayer antiferromagnetic coupling mediated by spin-polarized tunnel electrons between the two Fe electrodes through MgO layers as thin as 5 Å [83]. As shown in figure 11, where the coupling energy J is plotted versus MgO thickness, an antiferromagnetic coupling ($J < 0$) is measured for $t_{MgO} < 8$ Å, with a very fast increase of amplitude when the thickness of the spacer is reduced to 5 Å. Below this extremely low interlayer thickness, the occurrence of pinholes results in a direct ferromagnetic coupling. On the other hand, for larger spacer thickness (above 10 Å) a ferromagnetic coupling is always observed and ascribed to 'orange peel' interaction.

In this context we have explored the magnetic interaction between two magnetic elements separated by an epitaxial MgO insulator in continuous Co/Fe/MgO/Fe and FeCo/MgO/Fe structures grown by combined sputtering and laser ablation techniques [84]. In similar experiments to those recently reported by Faure-Vincent *et al* [83], SQUID measurements on three structures with fixed Co/Fe and Fe thicknesses and with MgO thicknesses of 20, 30 and 40 Å were performed. In both cases the individual Fe film acted as the soft magnetic layer with a smaller coercive field and either the FeCo alloy or the Co/Fe bilayer acted as

the hard magnetic counterpart. Regarding the morphology of the individual electrodes, AFM measurements were made *ex situ* for the different samples. In the case of the bottom Fe layer, a root mean square (rms) roughness of 3 Å was obtained. Additional evidence of atomically flat Fe/MgO/Fe interfaces can be extracted from HRTEM observations as reported in [48]. The 'orange-peel' type of coupling between both electrodes would be ferromagnetic for the case of roughness at the MgO/Fe bottom electrode interface, as it would produce correlated interface topography of both magnetic layers being conformal to the MgO growth. Since the layers are atomically flat this type of coupling in these heterostructures is expected to be negligible.

In figure 12(a) we show the loop for the Co/Fe/20 Å MgO/Fe structure with the magnetic field applied along the Fe[100] direction. An almost square hysteresis loop is observed, with 100% remanence and rounded corners, pointing to the likely presence of inhomogeneities in the sample, which produce a broadening of the experimental coercive fields. One single jump is observed in the magnetization reversal process, despite the different coercivities of top and bottom layers, indicating the magnetic coupling between them for this spacer thickness and lateral dimension of 5×5 mm^2. In figures 12(b) and (c) the hysteresis loops for similar structures, but with 30 and 40 Å MgO spacer thickness, are shown. For the 30 Å MgO sample the magnetization reversal proceeds in three stages, with two clear transitions at 50 and 400 Oe, and a rotation stage at intermediate fields characteristic of coupled media. This is probably because pinholes present in the 20 Å thick MgO spacer sample shown in figure 12(a) have almost completely disappeared in the 30 Å thick one. The hysteresis loop for the 40 Å thick MgO spacer shows two clear magnetization jumps at 50 and 450 Oe approximately, which indicates totally independent magnetic switching of top and bottom electrodes, with a large field window (∼300 Oe) where an antiparallel configuration is achieved. Taking into account the bulk magnetic moments of Fe (2.22 μ_B) and Co (1.72 μ_B per unit cell), as well as the nominal thickness of the electrodes, the expected value for the antiparallel alignment agrees very well with the experimental results if the lower coercive field corresponds to the bottom electrode and the higher coercive field to the top electrode magnetizations (see figure 12(c)).

Yet another important source of coupling between both ferromagnetic layers is that resulting from the large fringing fields surrounding magnetic domain walls in either of the layers, that can strongly influence the performance of future device applications. This interaction can for example originate magnetization decay in spin-dependent tunnel junctions [126], strongly modify the coercivity of such structures [127] and even induce a strong ferromagnetic coupling between both electrodes via the so-called domain duplication [128–130].

4. Structure and magnetic properties of patterned epitaxial Fe/MgO/Fe tilings

As discussed in the previous sections, continuous film TM/MgO epitaxial heterostructures display a rich variety of magnetic behaviours depending on the growth conditions. Notably, varying the growth temperature allows one to obtain from atomically smooth flat layers and interfaces to 3D island growth mode, observing a drastic effect on the magnetic properties. These facts make epitaxial Fe single layers and Fe/MgO sandwiched structures model systems to study interactions and transport phenomena in metal–insulator heterostructures, where well defined structure and interfaces implies well defined electronic states and well defined magnetic anisotropies at the metal, the insulator and the interfaces. In this section, we review the current understanding of magnetic interactions in arrays of artificially produced epitaxial TM and TM/MgO/TM tilings. Both single-layer and multilayer structures are considered. We pay special attention to the interactions in TM/MgO/TM tilings, which are arrays of ferromagnetic tunnel junctions, with considerable technological interest.

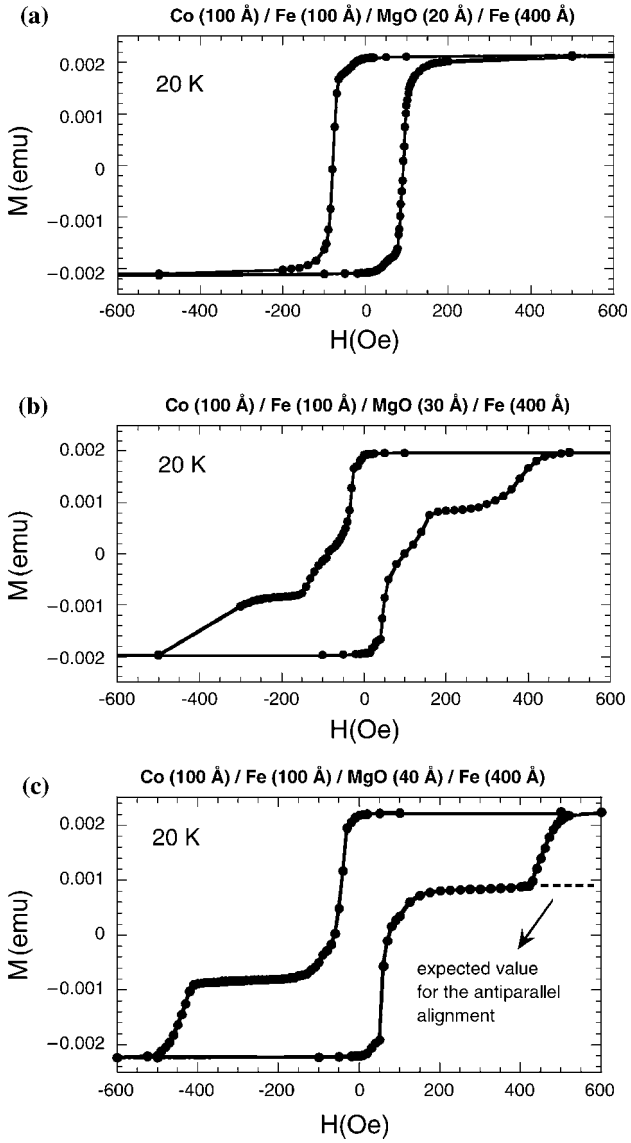

Figure 12. Magnetization loops at 20 K for 100 Å Co/100 Å Fe/MgO (d)/400 Å Fe heterostructures with varying MgO barrier thicknesses (a) $d = 20$ Å, (b) $d = 30$ Å and (c) $d = 40$ Å. Magnetic field was applied along the [100] Fe direction. The dotted line in (c) accounts for the estimated magnetization corresponding to the antiparallel magnetic configuration of both electrodes.

These ordered arrays of magnetic entities are interesting both to study the effect on magnetic properties of reducing size and to study their collective behaviour when there is interaction between neighbour elements. This interaction, as shown recently, can be used to propagate signals along magnetic nanostructure lines [131]. On the other hand, there is a considerable interest in studying magnetic properties of artificially produced arrays of magnets, since there is a fundamental stability limit reducing size in domains in flat recording media. In this area, both magnetic media with the magnetization perpendicular [132] to the film plane and

AFC disc media are extremely interesting [133]. Additionally, there is considerable interest in studying the properties of 3D stacks of magnetic elements separated by a thin insulating layer, since they open in principle the possibility of recording magnetic information which would be read by the resistance of the whole stack [13].

In what follows we review the literature on epitaxial magnetic heterostructure arrays, i.e., magnetic heterostructure arrays built with single-crystalline materials. The reader is referred to recent reviews [134, 135] for magnetic nanostructures fabricated with polycrystalline materials.

4.1. Fabrication and characterization of epitaxial tiling arrays

In order to fabricate patterns on a surface a key issue is lithography, a term involving several closely related techniques such as resist coating, exposure and development. Among the different lithographic techniques (e-beam, x-ray, interference or holographic, scanning probe, focused ion beam. . .) e-beam lithography has been the most frequently used to pattern epitaxial structures. This is because the arrays of epitaxial elements are preferably fabricated by post-growth lithography, defining a mask on top of the film that acts as a cover in a subsequent ion beam etching procedure. Although it is possible in principle to use lift-off techniques on epitaxial substrates (i.e., spinning the substrate, irradiating, developing, growing and lift-off), there usually remain small quantities of resin on the electron-exposed areas, degrading the quality of the growth structure and the interfaces. The reader can find details and further references about lithographic methods in [136].

The epitaxial nanostructure arrays fabricated to date are mostly built with Fe elements [47, 76, 137–161] but also with Co [143, 162–167], Ni [168] and different materials [169, 170]. The measurements reported include SQUID [154], AGM [153, 156, 167, 168], VSM [154, 163], torque [163], MOKE [47, 137, 139–141, 146–149, 159–161, 165], MO torque [157, 162], diffracted MO [161], STM [155, 166], AFM [137, 155, 158, 163, 167, 168], SEM [139, 141, 146, 149, 151, 153], MFM [138–145, 150, 151, 153, 162–165, 167, 169], scanning Kerr microscopy [148, 152] and magneto-transport [47, 138, 142–145, 147, 150, 155, 162, 164]. In addition, micromagnetic simulations [139, 140] and other theories [171] have also been reported in this context. The arrays are built with elements of different shapes such as squares [137, 158–161], stripes/wires [138, 142–150, 152, 157, 162, 166], dots/circular [151, 153, 154, 156, 163, 166–168, 171], particles/islands [140, 155] and other more complex (rectangular, triangular, elliptical, needle. . .) shapes [139, 141, 153, 167, 168].

Needless to say, amongst these characterization techniques, magneto-optic measurements are an invaluable and inexpensive tools when studying these patterned arrays. The advantages are considerable.

(I) Some of the structures discussed are unavailable to conventional magnetization measurements since the magnetic signal is extremely small.
(II) The effect of patterning can be studied in the same film where different patterns have been written by focusing the incident light inside the pattern. This rules out accidental effects due to the use of different samples grown, in principle, under the same conditions.
(III) When studying regular arrays of nanomagnets, light is not only reflected, but also diffracted by the array. Magneto-optics in diffracted beams opens a whole new area of interesting phenomena where one has experimental access to the magnetization inhomogeneities within the arrays [172].
(IV) The arrays can be excited easily not only with conventional magnetic fields (fixed direction varying amplitude) but with rotating magnetic fields (constant amplitude varying angle) as well, a technique called magneto-optical torque [173, 174]. This set-up eliminates

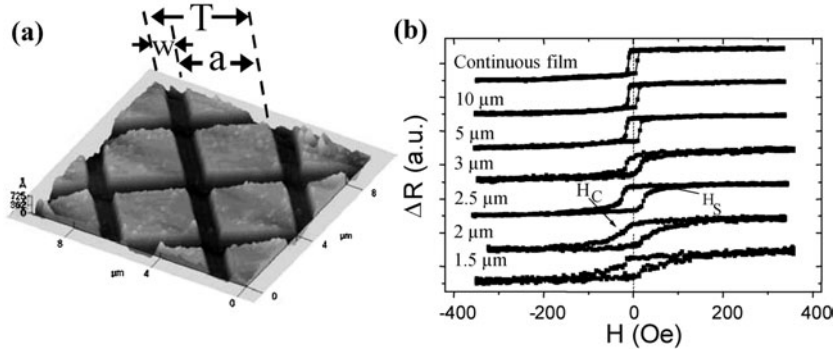

Figure 13. Epitaxial Fe(100) tiling. (a) AFM image showing the period T of the structure, the tile edge size a and the inter-tile separation w. (b) Hysteresis loops of arrays of different edge size; the top loop is the hysteresis loop of the continuous film, shown for comparison purposes. Magnetic field applied along the Fe[110] hard axis, taken from [137].

uncertainties due to domain wall movements when determining anisotropies, and, similar to conventional torque techniques, a single measurement and a small fit produce the symmetry and strength of the anisotropy axes.

(V) The information obtained when shining light on a magnetic array is statistical in the sense that it contains contributions from hundreds to hundreds of thousands of elements, depending on the relative size of the light spot and the magnetic element.

4.2. Arrays of single-layer elements

Before discussing the effect patterning has on epitaxial Fe/MgO/Fe heterostructures it is appropriate to understand the effect it has on single-layer continuous films. As mentioned before, and as expected, a continuous Fe film displays a magneto-crystalline anisotropy with easy axes along [100] directions [114]. In addition a small uniaxial anisotropy is found, most probably related to the MgO texture. On patterning an array of micro-squares there are two relevant distances, and, accordingly, two main effects on the magnetic properties of the array. One is the lateral size of the tile, a, and the other is the separation between them, w, as shown in figure 13(a). The magnetization of the array, measured as the transverse MOKE reflectivity changes, is shown in figure 13(b). The top loop is the unpatterned film and is shown for comparison purposes. Notice that patterning has a moderate effect on the magnetization of the array until a tile size threshold of about 3 μm. This occurs because, as the tile becomes smaller, demagnetizing effects become more relevant. As a result there is an increase of the magnitude of the external field required to switch the tile magnetization. This is observed in figure 14(a), where the coercive field for an array of Fe epitaxial tiles is displayed as a function of the tile lateral size. However, the individual tiles remain basically single domain, until the demagnetizing energy becomes comparable to the anisotropy energy. This happens when the tiles are about 3 μm in lateral size, and compares well with simple estimations for the size where anisotropy and demagnetizing energy contributions for Fe become comparable. Figure 14(b) shows an MFM image of a square tile of about 1.5 μm lateral size, where the breakage in domains of the magnetization distribution within the tile is quite evident.

The second aspect concerns the magnetic interaction between neighbour elements in magnetic nanostructure arrays with the magnetization in the film plane. This is related to the distance at which the magnetic elements are separated, w in figure 13. The interest is

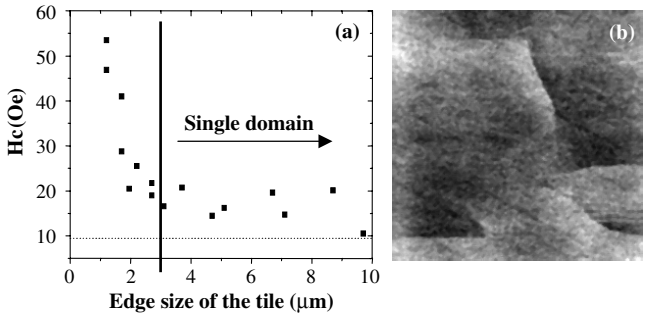

Figure 14. (a) Coercive field as function of the edge size for epitaxial Fe(100) tilings. Notice a threshold at about 3 μm size below which the coercive field increases dramatically. The horizontal dotted line corresponds to the coercive field for the continuous film. (b) MFM image (1.5×1.5 μm^2 scan) of a tile of about 1.5 μm edge, where the multidomained nature is clearly observed.

twofold; on one hand it is important to understand and quantify the interaction to avoid 'cross-talking' when recording information on magnetic arrays. This is valid both for single- and multilayer structures. On the other hand this same 'cross-talk' can also serve as a control parameter, where one can change an element magnetization (write one bit) through a line of interacting elements, build logic etc.

As an example we show in figure 15 the effect the lateral separation between elements has on the magnetization of an array of Fe(001) micro-squares. Measurements were made for periods of 7 and 9 μm, and tile separations of 0.3, 0.9 and 1.5 μm. When the tiles do not interact (figures 15(c) and (f)), a wall nucleation and propagation event is needed per tile. However, when the tiles do interact (figures 15(a), (b), (d) and (e)), the instant one tile switches magnetization it triggers the reversal of the whole array, as in an array of domino pieces. This is demonstrated by the abruptness of the magnetic transition at the coercive field. While in the interacting set of tiles there is an abrupt transition, there is a dispersion of nucleation fields in the isolated set of tiles. Notice that this measurement provides quantitative information on the distribution of nucleation sites as well.

The interaction between neighbouring tiles can be quantified by the deviations of the internal field that an isolated tile would experience. In other words, for an isolated tile one can calculate approximately the internal field (or the demagnetizing factor); this is shown by the continuous line in figure 16. When the tile is closer to another neighbour tile, some of the magnetic flux departs, decreasing this demagnetizing field, and consequently less field is required to saturate the tiling. The behaviour tends as expected, for infinitely close tiles, to the continuous film behaviour. Confirming this picture figure 16 shows the saturation field for similar arrays separated by 1.5 μm (hollow circles) and 0.5 μm (solid circles).

4.3. Arrays of multilayered elements

In order to fabricate MRAM it is important to understand and quantify the different phenomena involved when reducing size and placing in regular arrays micro-fabricated tunnel junctions. Specifically, it is necessary to know if it is possible to fabricate a stable antiparallel alignment of the magnetization and how. In spin valve materials used in recording heads this is achieved through exchange coupling of one electrode (the pinned layer), leaving the other layer free to switch. It is also necessary to understand and quantify the different anisotropies and changes in switching fields introduced by the patterning process. In what follows we describe, as an

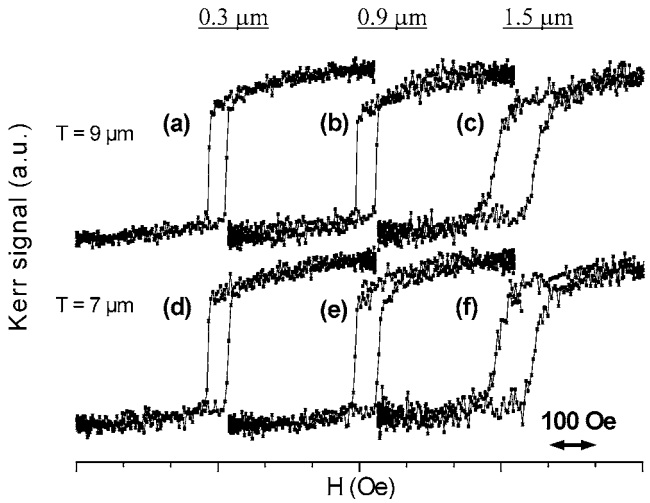

Figure 15. Hysteresis loops for epitaxial Fe(100) tilings with the same period but different inter-tile separations. Notice a sharp reversal at 0.3 μm inter-tile separation, indicative of a cascade switching of the array, while at 1.5 μm inter-tile separation there is a distribution of switching fields. Taken from [137].

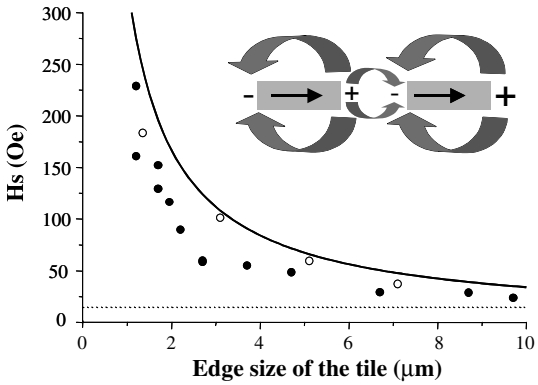

Figure 16. Saturation field for epitaxial Fe(100) tilings of different edge sizes. Empty circles represent a series with 1.5 μm inter-tile separations while solid circles correspond to 0.3 μm inter-tile separation. The solid curve is the demagnetizing field for an ellipsoid with the same aspect ratio. The horizontal dotted line corresponds to the coercive field for the continuous film. The inset schematizes the closing magnetic flux situation. Taken from [137].

illustrative example, experiments carried out at the authors' laboratory on Fe/MgO/Fe micro-tunnel junction arrays.

Continuous Fe/MgO/Fe(001) trilayer structures are patterned by e-beam lithography and ion beam etching, and the resulting array of square junctions is measured by focusing a light spot, about 100 μm diameter, within the square 250 μm edge array. The measured magneto-optical Kerr loop corresponds then to the behaviour of several hundreds to thousands of micro-junctions. As for single Fe layers, patterning has a drastic effect on the magnetic properties of the array, as shown in figure 17 for a 10 nm Fe/2 nm MgO/10 nm Fe structure. However the effect is quite different than for the single layer with an equivalent 20 nm thickness. While

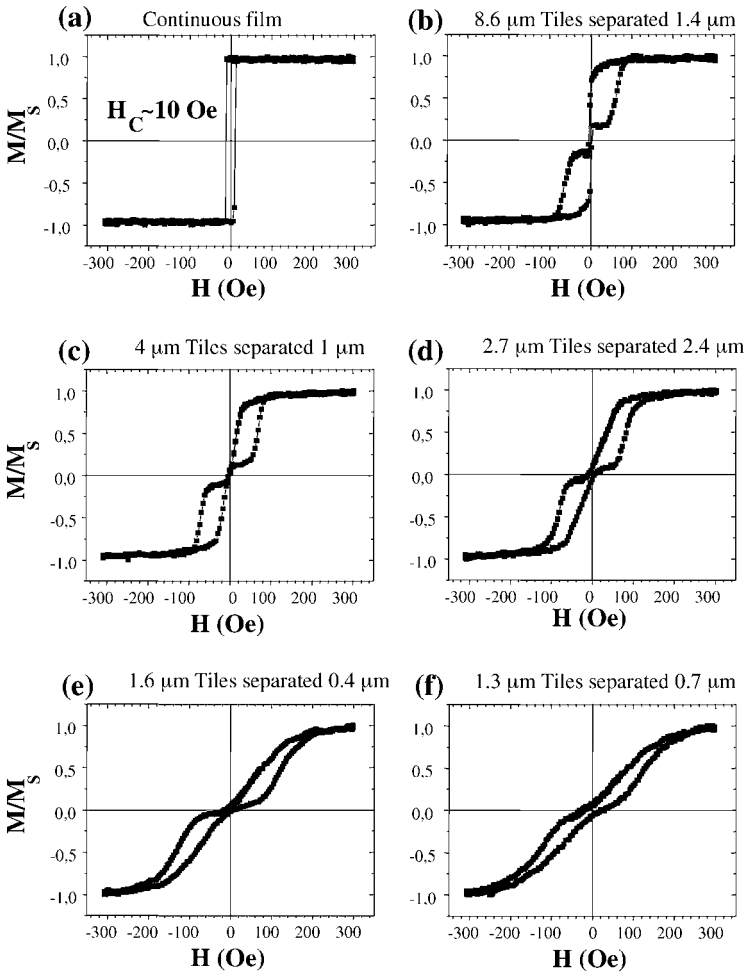

Figure 17. MO hysteresis loops for epitaxial Fe 10 nm/MgO 2 nm/Fe 10 nm tunnel junction arrays of different edge sizes and inter element separations: (a) loop for the unpatterned film; (b) loop for an array of junctions of $8.6 \times 8.6\ \mu m^2$ lateral size separated by 1.4 μm; (c) $4 \times 4\ \mu m^2$ junctions separated by 1 μm; (d) $2.7 \times 2.7\ \mu m^2$ junctions separated by 2.4 μm; (e) $1.6 \times 1.6\ \mu m^2$ junctions separated by 0.4 μm; (f) $1.3 \times 1.3\ \mu m^2$ junctions separated by 0.7 μm. Magnetic field applied along the Fe easy [100] direction. Taken from [170].

in the continuous structure (figure 17(a)) one single magnetization reversal event is observed, due to the equivalent coercive fields of both top and bottom magnetic layers, in the trilayer case a two-stage reversal of the magnetization, with remanence close to zero, is observed after patterning the continuous structure. The reversal starts at positive fields, a fact that needs a unidirectional 'type' of coupling, i.e., it cannot be explained with conventional bi-directional anisotropies. All this points to an antiferromagnetic coupling between top and bottom layers due to the magneto-static energy reduction. Simple magnetic balance calculations support this statement [170]. On the other hand, and similar to the single-Fe-layer tile observations, the main factor affecting magnetization reversal in this trilayer case is the lateral dimension of the micro-squares. The smaller tiles exhibit increasing switching field magnitudes and dispersions, although maintaining a two-stage reversal with overall zero remanence.

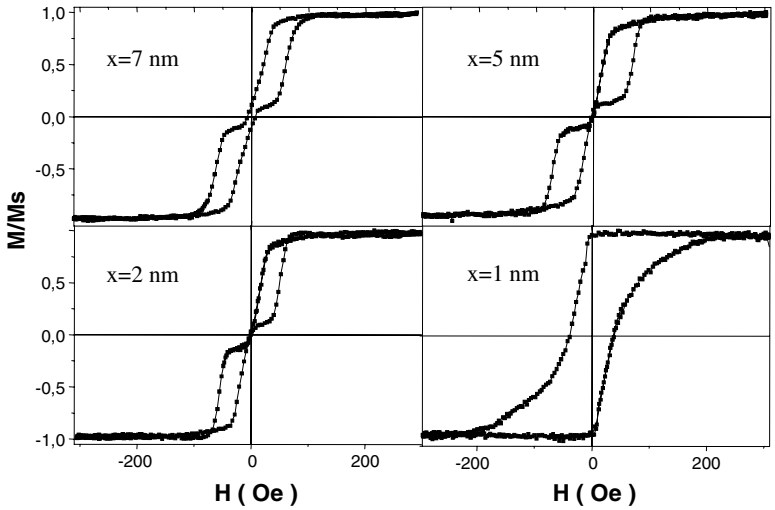

Figure 18. MO Kerr effect for arrays of epitaxial micro-tunnel junctions of approximately the same lateral size, about 3.5 μm, separated by about 1.5 μm and with different barrier thicknesses: 10 nm Fe/x nm MgO/10 nm Fe ($x = 7$, 5, 2 and 1 nm). Magnetic field applied along the Fe easy [100] direction. Taken from [170].

In addition, the effect of reducing the thickness of the epitaxial MgO insulator is shown in figure 18 for Fe 10 nm/MgOx nm/Fe10 nm tilings with square elements of about 3.5 μm side. As observed, this two-stage reversal of the magnetization disappears at 1 nm MgO thickness, which is about two unit cells. Notice as well that the saturation field increases in this case. This loop is very similar to the 200 Å single-layer Fe tiling of similar dimensions, which implies that the MgO barrier has collapsed and direct exchange has become effective between top and bottom electrodes in most of the tiles of the array. This probably means that the coverage for this thickness is not homogeneous and that some areas the two electrodes are in contact, the so-called pinholes. Exchange would become effective through these contact areas.

As mentioned before, the possibility of some coupling mediated through the electrons tunnelling between top and bottom ferromagnetic layers is investigated in [83], where Faure-Vincent *et al* find an antiferromagnetic type of coupling between Fe layers for MgO thickness lower than 10 Å in continuous films. In our case, for arrays of tunnel junctions with 1 nm MgO spacer, we find a behaviour very dependent on the lateral size of the junctions. Figure 19 shows selected hysteresis loops for arrays with different lateral sizes of the micro-junctions, with the field applied along an easy Fe[100] direction. The continuous macroscopic film displays a square loop (not shown in the figure) with a coercive field of 10 Oe, demonstrating the simultaneous reversal of top and bottom electrode magnetizations as in a single-Fe-layer film. For junctions larger than 3 μm (figures 19(a)–(d)), the reduced remanence, $M_R = M/M_S|_{H=0}$, of the array is close to one, pointing to top and bottom Fe electrodes that are exchange coupled. In other words, most of the array still behaves like the continuous film. However, for 3 μm junctions and smaller (figures 19(e) and (f)) the reduced remanence decreases, and loops demonstrate a reversal by two stages with a remanent state close to zero magnetization along the applied field direction. This indicates that the two electrodes' magnetizations orient in an antiparallel fashion for a large fraction of the array elements. For this barrier thickness, 10 Å MgO, the effect of patterning on the magnetic loops is different from what has been measured for 20, 50, and 70 Å MgO, where the two-stage magnetization reversal is measured for all lateral sizes, and explained by the magneto-static energy reduction obtained by the

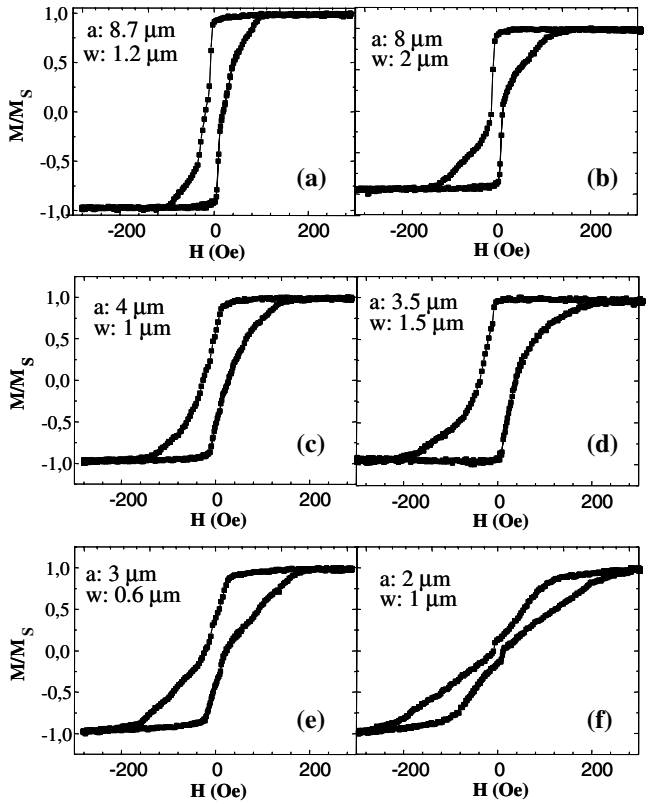

Figure 19. MO hysteresis loops for epitaxial Fe 10 nm/MgO 1 nm/Fe 10 nm tunnel junction arrays of different edge sizes and inter-element separations: (a) loop for an array of junctions of $8.7 \times 8.7\ \mu m^2$ lateral size separated by 1.2 μm; (b) loop for an array of junctions of $8 \times 8\ \mu m^2$ lateral size separated by 2 μm; (c) $4 \times 4\ \mu m^2$ junctions separated by 1 μm; (d) $3.5 \times 3.5\ \mu m^2$ junctions separated by 1.5 μm; (e) $3 \times 3\ \mu m^2$ junctions separated by 0.6 μm; (f) $2 \times 2\ \mu m^2$ junctions separated by 1 μm. Magnetic field applied along the Fe easy [100] direction.

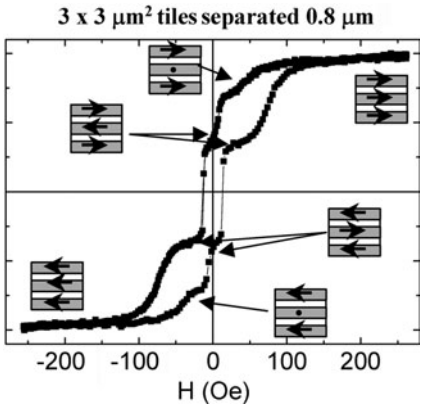

Figure 20. Hysteresis loop for an epitaxial Fe 6.5 nm/MgO 5 nm/Fe 6.5 nm/MgO 5 nm/Fe 6.5 nm tile array. The reflectivities of the sketched magnetization orientations (marked by the arrows; dots correspond to magnetization perpendicular to the page) have been calculated using the transfer matrix formalism. Magnetic field applied along the Fe easy [100] direction.

antiparallel orientation of the electrodes' magnetizations. All these experimental facts prove that pinholes in the barrier are the main cause of the observed behaviour. In this scheme, the system behaves as if there is a threshold number of pinholes (or pinholes of a certain size) above which the two electrodes are coupled ferromagnetically. Patterning the structure and decreasing the size of the elements decreases the number of junctions coupled via pinholes, increasing the area occupied by exchange uncoupled junctions. These data suggest the possibility of local antiferromagnetic coupling, of magneto-static origin, in junctions below 3 μm lateral size with barrier thicknesses lower than 1 nm.

Finally, the Kerr loop corresponding to an epitaxial heterostructure array built with three layers of Fe 6.5 nm thick, separated by 5 nm MgO (3 μm lateral size tiles separated 0.8 μm) with the magnetic field applied along the Fe[100] easy axis is shown in figure 20. Due to the multilayered nature of this structure, the analysis of its magneto-optical response is not obvious, mainly due to absorption and interference effects. The application of a transfer matrix formalism [175, 176] is necessary to determine the response of the overall structure depending on the relative orientation of the different Fe layers. For example, taking as a reference the 100% Kerr signal corresponding to the saturated state, i.e., the magnetization of the three layers are parallel, 180° reversal of the topmost layer yields a total Kerr signal of only 16% with respect to saturation. This is mainly because deeper Fe layers contribute less due to absorption effects on the top layers. In the same way, a reversal of the intermediate Fe layer keeping the other two parallel yields 30% of the total Kerr signal, and reversal of the bottom layer, 54%. With this formalism in hand it is possible therefore to identify the different magnetic configurations from the measured Kerr signal in the hysteresis loop. In figure 20 the different magnetic configurations of the three Fe layers are identified in the different regions of the loop according to the measured Kerr effect. As mentioned, saturation corresponds to 100% signal. Reducing the magnetic field leads to a metastable state at around 30 Oe where top and bottom Fe layers remain parallel, while the magnetization of the intermediate one has rotated 90°. This is reasonable since it corresponds to another magnetically easy direction of this layer. Further reducing the magnetic field down to zero leads to a stable structure for which the Kerr signal corresponds to an antiferromagnetic state, where the magnetization of the intermediate Fe layer is oriented antiparallel with respect to the top and bottom ones. In this antiferromagnetic state the magneto-static energy is minimized, conferring high stability to this configuration. This situation is demonstrated by the fact that applying a small magnetic field in the negative direction causes the reversal of the whole structure, maintaining the antiferromagnetic state. Further application of negative magnetic field finally forces the parallel alignment of the three layers' magnetizations, breaking this antiferromagnetic orientation.

As has been shown, this kind of new magnetic structure, with a wide combination of possible stable and metastable magnetic states, opens interesting possibilities, both fundamentally and for applications. They for example might have the potential to store magnetic information in 3D being read through the tunnel resistance of the whole stack or using magneto-optical methods.

These last two examples, magnetic couplings through insulating layers one or two unit cells thick, and magnetic interactions in epitaxial heterostructures, are from our point of view illustrations of research challenges where epitaxial systems are definitely desirable to fully understand the relevant physical mechanisms.

5. Transport and magneto-transport in epitaxial TM/MgO/TM heterostructures

This last section treats another relevant aspect of metal–insulator heterostructures: the transport properties. Recent breakthroughs in MTJs have triggered great scientific and commercial

interest, even though tunnelling is a phenomenon as old as quantum mechanics. It was in 1927 that Hund demonstrated [177] that a current can pass from one electrode through a thin insulating barrier into a second electrode, this electrode/barrier/electrode trilayered structure being referred to as a tunnel junction. The measured current is explained considering an electron that encounters a potential barrier: though most of the amplitude of the associated wavefunction will be reflected at the potential step, a portion decays exponentially into the barrier. For sufficiently thin barriers, there is a finite probability of finding the electron on the other side of the potential step.

Trying to understand tunnelling phenomena, the current, or its derivative, is measured as a function of applied bias voltage. At thermal equilibrium, electrons flow from one electrode to the other, equilibrating chemical potentials at each side of the barrier. A bias V across the junction raises by eV the Fermi level of one electrode with respect to the other, and there is a net flow of electrons tunnelling through the insulating layer. Although a complete conceptual background for electron tunnelling is beyond the scope of this review, we briefly point out that the number of electrons tunnelling from one electrode into another is given by the product of the density of states at a given energy in one electrode and the density of available states in the other electrode, weighted by the square of a matrix element describing the tunnelling probability. The net current is then the difference in the number of electrons tunnelling from one electrode to the other.

5.1. Early works and theories

Quantum tunnelling has remained a hot topic from its beginning, with a myriad applications to this day. Most of the early work on tunnelling was theoretical because of the lack of reliable experiments. Fowler and Nordheim [178] explained in 1928 the main features of electron emission from cold metals by high external electric fields on the basis of tunnelling through a triangular potential barrier. But it was not until 1957 that Esaki [179] found conclusive experimental evidence for tunnelling. In 1960 Fisher and Giaver [180] performed the first thoughtful attempt to fabricate a metal/insulator/metal tunnel junction by the use of vacuum evaporation techniques, in a fashion that has not changed much since then [24]. They obtained current–voltage (I–V) characteristics that agreed with theory, i.e., the conductance $\mathrm{d}I/\mathrm{d}V$ has a parabolic dependence, at low bias resistance is constant, and it has an exponential dependence on oxide thickness.

The next advance was the Meservey–Tedrow [1] spin-polarized tunnelling (SPT) experiments, measuring the spin polarization of the tunnelling current from a ferromagnetic electrode into a superconducting one. In most cases the insulating barrier was amorphous Al_2O_3 and, as shown in figure 28 of their paper [1], these experiments led to positive spin polarization for all materials measured with this technique (table 1). This finding contradicted the expectations based on the density of states for majority and minority spin populations at the Fermi surface for the ferromagnetic electrodes. The band structures for most ferromagnetic metals predicted negative spin polarizations, and positive values were found in all the experiments.

It was Simmons [181] who first solved the problem of the I–V relationship for a tunnel junction with a potential barrier of arbitrary shape. The equation derived for the tunnel effect has the advantage that it can be applied to any shape of potential barrier providing the mean barrier height and thickness are known, or alternatively, if the I–V characteristics of a tunnel junction are known, then barrier parameters can be obtained from a simple fit. Introducing the dielectric constant of the insulating film allows us to point out tunnel characteristics

Table 1. Polarization values for different ferromagnetic metals, taken from [1].

Metal	Spin polarization (%)
Fe	40 ± 2
Co	35 ± 3
Ni	23 ± 3
Gd	14 ± 3
Ho	7.5 ± 1
Dy	7 ± 1
Tb	6.5 ± 1
Er	5.5 ± 1
Tm	2.7 ± 1

as an intrinsic function of the thermal properties of the insulator, as well as those of the electrodes.

In the 1970s tunnelling between metals was not a field that could be regarded as fully understood [182]. The tunnelling current was supposed to be independent of the densities of states of the electrodes due to a normalization factor in the transition probability. This was experimentally supported by data for junctions with small Sn particles embedded in an alumina barrier [183]. Then, Jullière, using ferromagnetic electrodes, quantitatively estimated the TMR ratio in terms of the classical theory of tunnelling. This assumes that the magnetic electrodes are two completely independent systems and that the insulating barrier is a quantum perturbation. In other words, in the system FM/I/FM the difference between the conductances ΔG for parallel $G_{\uparrow\uparrow}$ and antiparallel $G_{\downarrow\uparrow}$ configurations of magnetization of the two FM electrodes is given by

$$\Delta G/G_{\downarrow\uparrow} = \Delta R/R_{\uparrow\uparrow} = 2P_1P_2/(1 - P_1P_2) \tag{1}$$

where P_1 and P_2 are the spin polarizations of the two ferromagnetic electrodes.

Moreover, the polarization P is given in terms of the density of states $N^*(E_F)$ at the Fermi energy E_F of the ferromagnet by

$$P = N^{\uparrow}(E_F) - N^{\downarrow}(E_F)/N^{\uparrow}(E_F) + N^{\downarrow}(E_F), \tag{2}$$

where both up- and down-spin electrons are supposed to proceed through two independent channels in order to guarantee spin conservation during the tunnelling process.

Despite the remarkably predictive success of Jullière's formula, it can foretell neither the dependences of the tunnelling magneto-resistance effect on the thickness and height of the insulating barrier, nor complex situations such as double-junction systems, the effect of impurities in the barrier or even the role of inserted non-magnetic interlayers between one of the ferromagnetic electrodes and the barrier.

In a continuous description, Slonczewski [119] treated the electrodes and the barrier as a single quantum system. When the barrier is relatively permeable the evanescent wavefunctions of electrons from both electrodes overlap in the barrier region and for that reason need to be matched across the whole structure. He described both ferromagnetic electrodes by two parabolic bands (one for each spin direction) shifted with respect to one another due to the exchange splitting. The polarization for each spin current is then identified as

$$P = (k^{\uparrow} - k^{\downarrow}/k^{\uparrow} + k^{\downarrow})(\kappa^2 - k^{\uparrow}k^{\downarrow}/\kappa^2 + k^{\uparrow}k^{\downarrow}), \tag{3}$$

where k^* is the Fermi wavevector, (*) extended to each spin channel ($\downarrow\uparrow$). Because parabolic bands satisfy $k^* \propto N^*(E_F)$ the polarization P given by equation (3) simply reduces to equation (2) for a large barrier height. In addition, one artifact of the parabolic band model

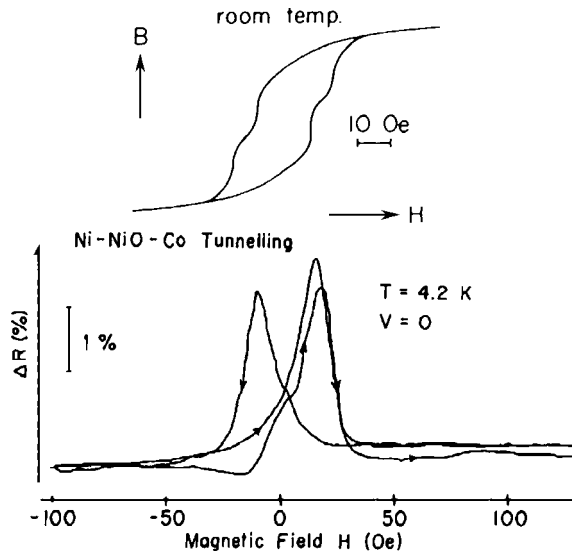

Figure 21. Magneto-resistance of a Ni/NiO/Co junction versus magnetic field, together with the corresponding B–H hysteresis loop. From [186] ©1982 IEEE.

is that P changes its sign as long as the barrier becomes lower. These results contradict the idea that a quantity like polarization is characteristic of the electrode band structure alone and would have the same value in any tunnelling experiment [184, 185].

In Jullière's model, the transmission probability is assumed to be constant and independent of the k^* on each side of the barrier. However, following Slonczewski's calculation, the tunnelling conductance depends not only on spin-dependent densities of states of both ferromagnets, but also on the spin dependence of the transmission probability. Nevertheless this model does not consider more realistic problems such as barrier non-uniformity, electron–electron correlations, crystal potential, spin waves and inelastic tunnelling.

The first report on magneto-resistance ascribed to tunnelling (TMR) was due to Jullière in 1975 [23] for an Fe/Ge/Co junction with an oxidized amorphous Ge barrier. Promising TMR values were shown to be as high as 14% at 4.2 K, as depicted in figure 2 of his paper [23]. Despite the fact of not being yet reproduced, these results opened an exciting research topic. As a result, as shown in figure 21, Maekawa and Gäfvert [186] unambiguously correlated the hysteresis behaviour of the magnetic electrodes in Ni/NiO/Co junctions with the observed magneto-resistance (2% at 4.2 K), establishing for the first time that the magneto-resistance effects were due to the relative magnetization alignment of the electrodes. These results were independently reproduced by Suezawa and Gondo [187], and later by Kabani *et al* [188]. On the other hand, Nowak and Rauluszkiewicz [189] measured the hysteresis of the tunnelling resistance of GdO_x-based tunnel junctions with Gd and Fe electrodes, and attributed the magneto-resistance not to the transition from parallel to antiparallel alignment of the magnetic electrodes, but to a spin-filter effect in the GdO_x barrier. Nevertheless, these effects were small compared to those anticipated from Jullière [23], and problems such as 'Néel orange-peel coupling' [190, 191], spin scattering within the barrier and pinholes were claimed to limit the number of appropriate materials to form a 'good' barrier. In fact, it was necessary to wait until 1995 when reproducible magneto-resistance ratios of over 15% at RT were reported in Fe/Al_2O_3/Fe [192] and CoFe/Al_2O_3/Co [193] junctions.

Since then, the most commonly used material for barrier fabrication because of its wetting properties has been Al, which is usually oxidized *in situ* to form amorphous Al_2O_3. Unfortunately for these junctions the oxidation parameters directly affect the device performance through spin-flip scattering: under-oxidation leaves some metallic Al and over-oxidation results in an additional oxide layer on the base electrode.

On the other hand, and despite amorphous alumina being the most widely used barrier, even a crystalline Al_2O_3 barrier was reported [194]. Among other examples of barriers used in MTJs are polycrystalline magnetic oxides like NiO [195, 196], CoO [197–199] and CrO_2 [195], amorphous nitrides like BN [200], AlN and AlON [201], polycrystalline HfO_2 [197], Gd_2O_3 [202] and Ga_2O_3 [203], amorphous Ta_2O_5 [184, 197, 204] and SiO_2 [194], epitaxial $SrTiO_3$ [205, 206], $NdGaO_3$ [207] and $CaTiO_3$ [208] and epitaxial semiconducting barriers like AlAs [209, 210], ZnSe [26] and polycrystalline ZnS [211].

5.2. Epitaxial ferromagnetic tunnel junctions: theoretical approaches

Since all previously mentioned conductance features seem to depend both on tunnel junction materials and growth methods, it is interesting to examine simpler systems by replacing the real insulating barrier with a vacuum spacer or to model experiments on epitaxial tunnel junctions with a crystalline insulating barrier. The advantage of these simpler systems is that *ab initio* calculations are now possible.

In this way, calculations of the electronic structure and the spin-dependent transport of single-crystal MTJs based on fcc Co(001) either with a vacuum gap [212, 213], Al_2O_3 [214] or $SrTiO_3$(001) [215] barriers have been reported. The calculated spin polarization for Co electrons tunnelling through a vacuum gap is positive and in excellent agreement with the experimentally observed value of $P \approx 35\%$ [1]. Similarly, the positive sign of spin polarization and TMR on tunnelling from cobalt across alumina was ascribed to different decay rates for the majority- and minority-spin electrons inside the Al_2O_3 barrier. In contrast, an exchange coupling was found between the interface Co and Ti atoms mediated by oxygen, which results in an induced magnetic moment on the interfacial Ti atoms and may explain the negative spin polarization of tunnelling across the $SrTiO_3$ barrier.

By self-consistent local spin density calculation within the Layer–Korringa–Kohn–Rostoker (LKKR) technique and atomic sphere approximation, MacLaren *et al* [216] first studied the generic Fe/barrier/Fe(001) system with a simple step barrier of varying height and width. They found that the conductance shows features not well described by any free electron picture and that, for a given barrier height, the conductance (or magneto-resistance) ratio is almost independent of barrier thickness and much larger than any experimental values ever reported.

Using the Landauer–Büttiker formalism that expresses the conductance as a sum of the transmission probabilities over different Bloch states, tunnelling conductance between Fe(001) electrodes separated by semiconducting ZnSe was described [217]. In particular, a large spin asymmetry in the tunnel conductance that increases with the barrier thickness was found along the (001) direction but not in other high-symmetry crystal orientations. This spin asymmetry was related to decaying metal-induced gap states (MIGS), i.e. near a crystal ferromagnet surface or interface one can match a wavefunction of complex $\boldsymbol{k}$ with one outside the crystal. Thus surface or interface evanescent states extended into the barrier also represent solutions of the bulk Schrödinger equation. To investigate the importance of MIGS for the tunnelling of metal electrons through epitaxial barriers, Fe/I/Fe(001)-based tunnel junctions, where I refers to semiconductor barriers Si, Ge, GaAS and ZnSe, were computed [218]. It was found that in all four cases the decay parameter is minimized at the Γ point ($\boldsymbol{k}_{\parallel} = 0$), consequently

the state $k_{\|} = 0$ will penetrate into the insulator farther than any other. In addition to the above semiconductors, they also considered that MgO would present the same behaviour for the reason that the band structure of MgO has the same topology as that of GaAs and ZnSe, tunnelling being determined predominantly by the Δ_1 states.

Recently, Fe/MgO/Fe(001) tunnel junctions were separately studied both by Butler *et al* [219] and Mathon and Umerski [220]. The method of Butler *et al*, based on matching wavefunctions across the barrier, shows that despite a negative spin polarization on the interfacial Fe layer, the spin polarization of tunnelling electrons should be positive. Furthermore, they illustrate that the symmetry of the Bloch states at the Fermi energy and their relationship to the symmetry of the slowly decaying evanescent states in the barrier layer are decisive to understand tunnelling conductance. Due to the different decay rates within the barrier for Bloch states of different symmetry, there will be more than one of these evanescent states in the barrier layer at E_F. Consequently Butler *et al* claim that it is possible that tunnelling will be affected by interference between these states, leading to an oscillatory dependence on barrier thickness as shown in figure 22.

This way, conductance in the parallel alignment of Fe(001) electrodes is dominated by the majority-spin channel with a broad peak centred at $k_{\|} = 0$. As depicted in figure 22, as the barrier layer becomes thicker the highest transmission occurs closer to the origin of the 2D Brillouin zone due to the slow decay in the MgO of Fe states from the majority Δ_1 band. Since the slowest decay rate is for states with Δ_1 symmetry, not existing in the minority channel, the magneto-resistance will then increase with the thickness of the barrier.

In a different way, Mathon *et al* describe the band structure of the electrodes and the barrier by tight-binding bands fitted to *ab initio* band structures of bcc Fe and bulk MgO, neglecting lattice distorsions. The on-site potentials in the Fe interface planes were adjusted self-consistently and the tunnelling conductance was evaluated in the low-bias regime using the Kubo formula in terms of the one-electron Green function at the Fermi surface. They found that TMR initially oscillates with MgO thickness, but from figure 23(a) it is clear that after seven atomic planes of MgO, it stabilizes and increases slowly, reaching values as high as 1200% for 20 atomic barrier planes. Figure 23(b) illustrates that the calculated spin polarization of the tunnelling current is always positive, because the majority-spin conductance is higher than the minority-spin conductance. When the magnetization of both electrodes is parallel, the majority-spin conductance is dominated by the Γ point, with also four subsidiary maxima in the 2D Brillouin zone along $k_x = k_y$. However, for the minority-spin channel or when both electrodes have antiparallel magnetization alignment, the conductance is determined by a ringed area with a minimum at the Γ point. This fact leads to large peaks ('hot spots') in the conductance for small MgO thicknesses, dissimilar in origin to those reported in [221]. As the MgO barrier becomes thicker, the contributions from the parts away from the Γ point are weakened and this is the reason why the TMR ratio becomes higher with barrier thickness reaching the asymptotic regime depicted in figure 23(a).

As described, in the case of Fe/MgO/Fe(001) similar conclusions are obtained individually. Both papers [219, 220] emphasize the role of interface quality but also the importance of symmetry of the junction as pointed out by Uiberacker and Levy [222]. Accordingly, tunnelling rates are higher if there are similar or identical states on both sides of the barrier, because the tunnelling electrons need not only to get through the barrier but there must be a state of the correct symmetry on the other side to accept them. As an example, Zhang and Butler [223] have demonstrated that the presence of an FeO layer in the Fe/FeO/MgO/Fe(001) system can reduce the TMR ratio from 4600 to 74% with respect to the symmetrical case due to a decrease in the majority channel conductance. In the same fashion, Wortmann *et al* [224] have recently developed conductance calculations for the totally symmetrical Fe/FeO/MgO/FeO/Fe case.

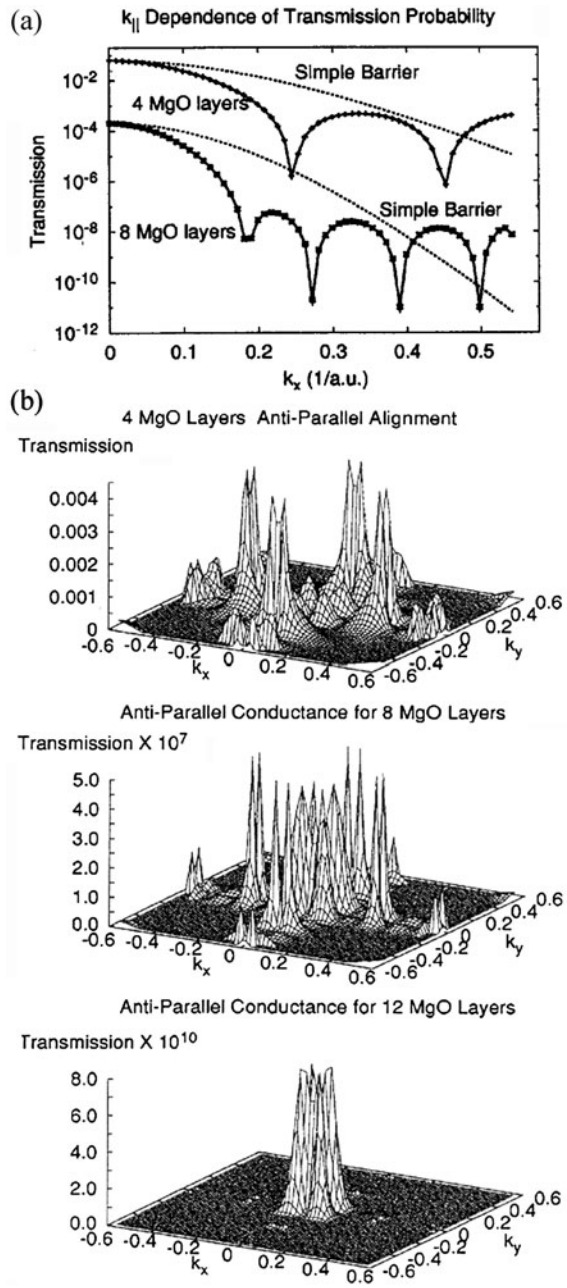

Figure 22. (a) Oscillatory majority transmission probability as a function of $\boldsymbol{k}_{\|}$ for $k_y = 0$ for four and eight layers of MgO for Fe/MgO/Fe(001) tunnel junctions. (b) Conductance for antiparallel alignment of the moments in the Fe electrodes for different MgO thicknesses, from [219].

This symmetry influence may be part of the explanation of the commonly observed decrease in TMR with bias for the reason that as the bias increases, the states on opposite sides of the barrier differ more. A comparable effect might be the presence of interfacial roughness and the formation of midgap states, which results in spin relaxation at the barrier surfaces and Fermi

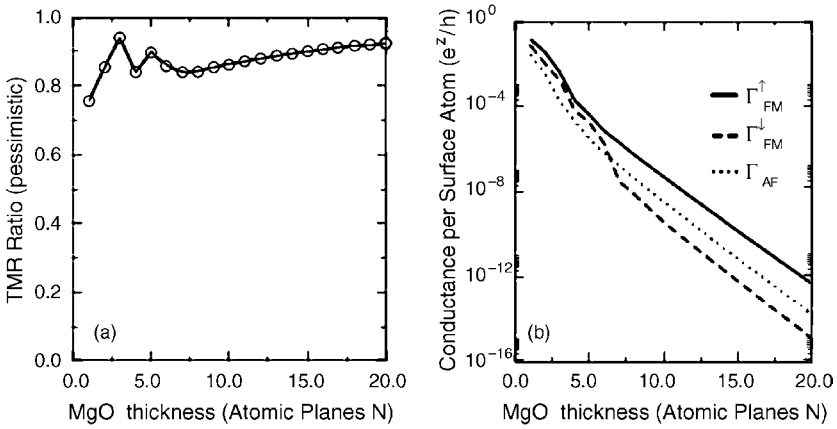

Figure 23. (a) Dependence of TMR ratio on MgO thickness for Fe/MgO/Fe(001) tunnel junctions. (b) Dependences of the total conductances for parallel Γ^{FM} and antiparallel Γ^{AF} configuration of the magnetization of two Fe electrodes on MgO interlayer thickness, taken from [220].

level pinning [225], with deviations from linearity on applied bias. Besides, the detailed nature of the symmetric Fe/MgO interface, nominally equivalent, might exhibit different properties in actual devices. For example in Fe/MgO/Fe and FeCo/MgO/Fe tunnel junctions exhibiting tunnel magneto-resistance [76, 82] the MgO/Fe interface is formed during MgO deposition at elevated temperatures on annealed Fe. On the other hand the Fe/MgO and FeCo/MgO interfaces are formed during Fe and FeCo deposition at RT on a well formed, stable MgO(001) surface, and therefore both interfaces structures might differ. According to [49], a c(2×2) RHEED reconstruction emerges on annealed Fe thin films as indicative of an atomically flat surface. A remaining open question is whether this c(2×2) rearrangement of the Fe atoms on the uppermost layer will endure after the MgO barrier deposition. This reconstruction is presumed to generate surface states different from localized d-like states originating from minority bands in the bcc (001) (1×1) Fe surface [49], and therefore transport characteristics in this case would be different from those calculated in [219, 220].

5.3. Epitaxial TM/MgO/TM magnetic tunnel junctions: experimental results

To experimentally test the previously described theoretical models, single-crystal structures are needed, and subsequently MgO barriers are becoming of increased interest because of the well established epitaxy of [MgO/Fe](001) superlattices [48].

MgO has previously been used as an insulating barrier in superconducting tunnel junctions, specially with NbN electrodes, since the 1980s. It was first used in amorphous [226] and polycrystalline states [227], but also in epitaxial form helped by their common structure and a low lattice mismatch [228]. These aforementioned MgO barriers were grown either by rf sputtering an MgO target in Ar atmosphere [226], rf sputtering of a MgO target in N_2 atmosphere [229], laser ablation of a Mg target in an oxygen environment [230] or by ion-beam oxidation from a Mg source [227]. Different crystallographic growth directions (001), (011) and (111) were achieved, keeping the deposition temperature as an experimental variable in order to control the thickness uniformity that arises from the tendency of an epitaxial layer to grow as a 2D or 3D layer. Tunnelling characteristics of these NbN/MgO/NbN Josepshon junctions were compared with those of Al_2O_3-based junctions, and barrier properties were checked depending on its epitaxial or polycrystalline nature, finding improved characteristics

for the epitaxial MgO case [228]. Furthermore, MgO has demonstrated excellent properties as a diffusion barrier with thermal stability up to 800 °C and good electrical insulation characteristics in layered systems [231].

On the other hand, from the basic point of view, and regarding MTJs, the availability of electrodes of the same material is very convenient, since the interpretation is much easier. Therefore, to impose a different magnetization reversal in one magnetic layer with respect to the other, it is necessary either to slightly vary the composition of the electrodes in order to change the coercive field, to deposit additional layers that antiferromagnetically pin one of the electrodes or to couple one of the electrodes to auxiliary ferromagnetic layers but with different switching fields.

As a simple approach, single-crystalline $Fe_{50}Co_{50}$/MgO/Fe(001) systems have been deposited on semiconductor GaAs substrates. Once a trilayer had been processed by optical lithography, Bowen *et al* [76] found a TMR of 60% at 30 K for a 20 Å MgO barrier. As the temperature increases, the TMR decreases in almost linear fashion to 27% at RT. The non-linear $I(V)$ dependence shown in figure 24(a), and the saturation of the resistance at low temperatures as demonstrated in figure 24(b), with a slow decrease between 50 and 300 K, served to identify good tunnel characteristics [232]. From the $I(V)$ temperature dependence it was possible to estimate the barrier height to be $\phi = 0.9$ eV, in good agreement with the fit to Simmon's equation that yields $\phi \sim 1.1$ eV for a barrier thickness of 15 Å. The TMR bias dependence was found to be almost symmetrical, reaching zero values at around 1.2 eV as shown in figure 24(c). From this bias dependence, and matching previous results on alumina barriers, the authors concluded that s-character electrons are predominantly tunnelling in the case of a 20 Å MgO barrier.

A second advance was to make magnetically harder the top Fe layer by adding Co, that is known to epitaxially grow on Fe. Using MBE, Popova *et al* [82] reported single-crystal Co/Fe/MgO/Fe (001) tunnel junctions on MgO(001) substrates. They observed a net TMR signal of about 15% at RT for a 10 Å MgO barrier. Unfortunately, no tunnel magneto-resistance dependence on bias was shown in this paper to support the previously concluded s-character of tunnelling electrons. From the tunnelling model of Brinkmann, they estimated a barrier height of 1.35 eV that was sustained by interlayer magnetic coupling experiments down to 5 Å MgO spacer, where a 1 eV barrier height was used in order to model the experimental coupling strength [83]. These results are in good agreement with previous transport studies using either polycrystalline MgO by Moodera and Kinder [233] or epitaxial MgO(111) by Kiyomura *et al* [234], who report $\phi \sim 0.9$ eV in the thickness regimen 10–30 Å. A somewhat higher value of ϕ has been reported by Wulfhekel *et al* [80] through STM local-probe measurements of MgO/Fe(001) structures, in which both the MgO and the vacuum barriers were taken into account. Recently, Klaua *et al* [81] have found the MgO bandgap to increase from 5.0 to 7.6 eV as the MgO barrier thickness varies from 2 to 6 ML, and therefore they estimate the barrier height to depend on the MgO thickness, reaching a value of 3.6 eV for thickness up to 6 ML. These results agree with those of Schintke *et al* [71] who showed that even for the case of 3 ML MgO on Ag(001) a bandgap of about 6 eV is observed, corresponding to that of the MgO(001) single-crystal surface. Nevertheless *ab initio* calculations of Butler *et al* [219] for the Fe/4 ML MgO/Fe(001) system predicted a bandgap of 5.5 eV which would roughly correspond to a barrier height above 1.3 eV, if we use the measured energy difference of 4.2 eV between the upper Mg 1s/O 2p valence band edge and the Fermi level of Fe [80]. Anyway, the lower barrier height values reported each time real tunnel junctions are used may account either for the integration of the barrier parameters over larger areas in contrast to STM experiments, or for the departure from ideality when comparing with theoretical simulations, since the presence

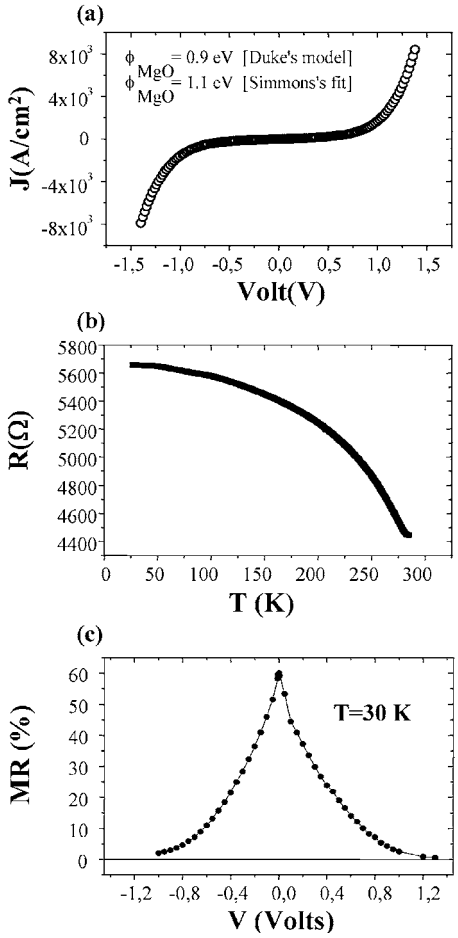

Figure 24. (a) Current–voltage characteristics with the estimated barrier height value, (b) temperature dependence of the resistance $R(T)$ and (c) bias dependence of the magneto-resistance for a 10 μm diameter FeCo/20ÅMgO/Fe(001) tunnel junction, taken from [76].

of stoichiometric disorder, thickness inhomogeneities or MIGS in the MgO barrier cannot be ruled out.

Remarkably, the low-temperature TMR value reported by Bowen *et al* [76] is in good agreement with expectations from Jullière's formula. Taking into account polarization values measured for polycrystalline iron ($P_{Fe} = 45\%$) and the iron–cobalt alloy ($P_{Fe_{50}Co_{50}} = 51\%$) [235] in SPT experiments with amorphous alumina barriers, a TMR $= 60\%$ is expected for the $Fe_{50}Co_{50}$/I/Fe case, decreasing down to 51% for the Fe/I/Fe type junctions. Nevertheless, lower values were anticipated for epitaxial Fe(001) since Yuasa *et al* [236] observed a strong anisotropic spin polarization of Fe depending on crystallographic orientation, as shown in figure 25. Using single-crystal Fe(001), Fe(011) and Fe(112) electrodes in semi-epitaxial $Fe_{50}Co_{50}/Al_2O_3$/Fe structures, they found the largest TMR $= 42\%$ for Fe(112) but only 13% for Fe(001). They calculated the spin polarization of the density of states (DOS) for the Fe(001) surface to be 4%, whereas from the TMR value the Fe(001) spin polarization appeared to be close to 12%, in clear contrast with the minor contribution from crystal directions to polarization values as measured through de Haas–van Alphen techniques [1]. The

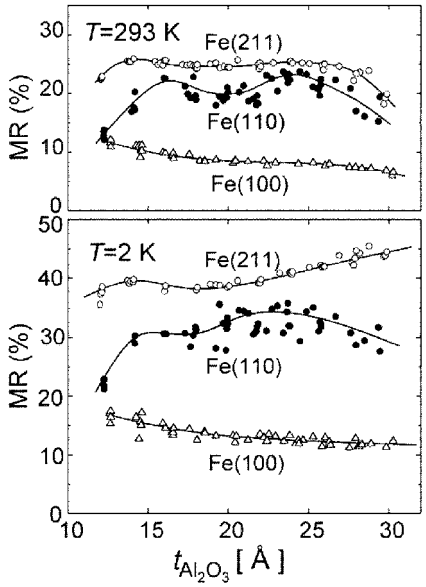

Figure 25. TMR ratios for different bottom electrode crystalline orientations, as a function of Al_2O_3 thickness in $Fe_{50}Co_{50}/Al_2O_3$/Fe junctions at 2 and 293 K. The Fe layer is a single crystal with (100) (triangles), (110) (solid circles) and (211) planes (hollow circles). Taken from [236].

demonstrated TMR dependence was ascribed to the details of the Fe band structure and the 'momentum filtering effect' of the alumina barrier (tunnelling probability as a function of the electron incidence angle is dependent on barrier thickness). On the other hand, an alternative explanation could be a slightly different growth mode of the amorphous alumina barrier on the different crystalline Fe facets, resulting in different barrier quality for each electrode crystalline orientation. The higher TMR value reported by Bowen *et al* [76], using an Fe(001) electrode as well, reveals that the spin polarization of tunnelling electrodes cannot be directly linked to the spin-polarized DOS of the free metal surface, but depends on the actual electronic structure of the barrier/electrode system and seems to be different for amorphous-Al_2O_3/Fe(001) and MgO(001)/Fe(001) interfaces.

Unfortunately, no experiments with variable MgO barrier thickness have been completed in order to prove the predicted relative increase of TMR with MgO barrier thickness [219, 220]. Still, these experiments show great promise for observing novel transport behaviour but also for making a detailed evaluation of the simplistic Jullière model, with no band structures or momentum filtering effects. In this way, epitaxial Co/MgF_2/MgO/Fe(001) tunnel junctions were recently reported [237], resulting in TMR of about 10% at low temperatures, which shows the actual progress in this research area. Obviously, and due to the growing interest in epitaxial systems, these results will be extended in future investigations.

5.4. Key aspects and open questions in epitaxial magnetic tunnel junctions

The actual magnitude of TMR, which is important for better performance of spintronic devices, is primarily determined by the spin polarization of the tunnelling current from the ferromagnetic metal–insulator interface. According to the positive polarization values obtained by Meservey and Tedrow, and following equation (1), only TMR positive values are expected. But when Sharma *et al* [184] found inverse TMR in NiFe/Al_2O_3/Ta_2O_5/NiFe composite barrier junctions

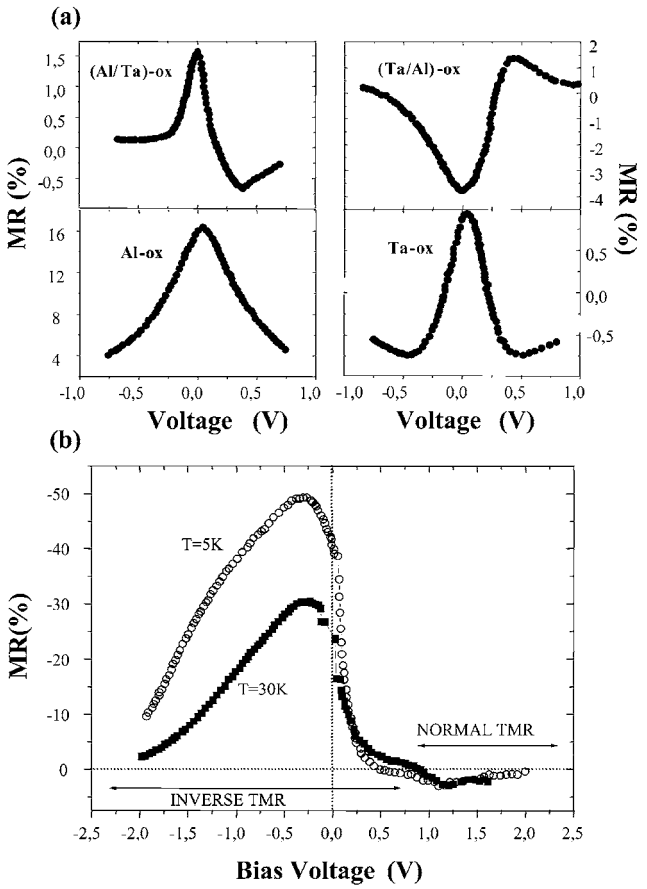

Figure 26. (a) Differences in the TMR-bias dependence for tunnelling junctions with Ta oxide and composited [Ta/Al] oxide barriers and NiFe and FeMn electrodes. After [184]. (b) TMR ratio as a function of applied dc bias for Co/STO/LSMO junctions. Taken from [185].

whereas values were positive in NiFe/Al_2O_3/NiFe junctions (figure 26(a)), and when de Teresa *et al* [185] reported an inverse TMR in the Co/$SrTiO_3$/$La_{0.7}Sr_{0.3}MnO_3$ system with a strong bias dependence (figure 26(b)), it was clear that the spin polarization in equation (1) is not a fundamental property of the ferromagnet but is interpreted as the spin polarization of the particular magnetic-material/insulator interface. In fact, it seems to be heavily influenced by the electronic structure and thickness of the barrier as well as by the barrier–electrode interface [86].

It is known that the quality of the interface between the ferromagnet and the insulator plays a crucial role in the value of the measured polarization; the use of improved techniques has led to an increase in the reported values of P_i [1]. In that fashion there are still remaining questions like the anisotropy of the spin polarization along different crystallographic directions [236], the apparent proportionality between the value of P_i and the saturation magnetic moment M of the ferromagnet [1] and the dependence of the polarization values on the artificial barrier used in addition to the effect of using well controlled epitaxial structures. On the other hand, no unique explanation for the temperature and voltage dependences of conductance and TMR have been assumed so far [238].

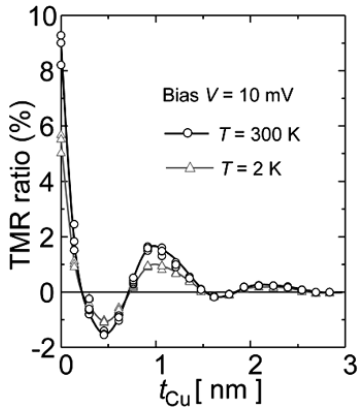

Figure 27. Oscillating TMR dependence as a function of the Cu layer thickness inserted in NiFe/Al_2O_3/Cu/Co(001) tunnel junctions. Reprinted with permission from [245] ©2002 AAAS.

Another aspect that can dramatically modify transport and magneto-transport in MTJs are defects and disorder. Real junctions contain large amounts of disorder in the barriers as well as at interfaces with electrodes. The simplest type of disorder may be non-correlated interface roughness, leading to fluctuations in barrier thickness. In this case the local electronic structure does not deviate much from that of an ordered structure. However, due to the strong dependence of tunnel conductance on thickness of the barrier [119], those areas, the so-called 'hot spots', which have smallest barrier thickness, contribute largely to the total junction conductance. This effect can be considered by a junction effective conductance with a reduced thickness of the barrier. Other forms of disorder, such as chemical due to interdiffusion, dislocations, stacking faults and vacancies at interfaces, influence the conductance in more complicated ways for the reason that DOSs at non-ideal interfaces are significantly altered. This makes the understanding of the intrinsic mechanism of TMR more difficult, since the resultant conductance is the average over many local disorder configurations with plenty of parameters involved [221, 239–241] in electron transport through resonances with localized electronic states in the barrier. The reader is referred to [242] for detailed analysis on the influence of the barrier parameters on magneto-resistance and on its bias dependence, as well as [243] for a topical review in spin-dependent tunnelling.

Additional advances come from novel ferromagnetic semiconducting structures, based on epitaxial *III–V* heterostructures. A pioneering work due to Tanaka and co-workers [209, 210] used AlAs barriers with $Ga_{1-x}Mn_xAs$ electrodes (different Mn concentrations yield different coercitivities). They observed a strong TMR dependence on barrier thickness that may account for a strict $\boldsymbol{k}_{\parallel}$ conservation. Straightforward integration with existing semiconductor technology and the fabrication of epitaxial heterostructures via molecular beam deposition techniques allows further tests of existing tunnelling models.

Even more interesting is the prediction [244] that whenever states in the barrier have a nonzero polarization, tunnelling magneto-resistance should occur even if only one electrode is ferromagnetic. In this way, recent experiments [245] revealed an oscillation of the TMR as a function of the thickness of a fully epitaxial non-magnetic metallic Cu(001) interlayer. This was inserted between the insulating barrier (a-Al_2O_3) and one of the ferromagnetic electrodes (Co(001) and NiFe) (figure 27) and interpreted in terms of spin-polarized resonant tunnelling due to quantum well states formed in the nonmagnetic interlayer. Clearly, further magneto-transport effects arising from quantum confinement in thin epitaxial interfacial layers are expected to occur within this new and exciting research area.

6. Summary

The most important aspects of the fabrication and the structural and magnetic properties of epitaxial metal–insulator heterostructures, with a special focus on the Fe/MgO(001) system, have been described. Results obtained both at the authors' laboratory and from other groups have been presented. This has included continuous, spontaneously organized and also lithographically processed Fe single layers and Fe/MgO multilayers, all of them (001) oriented. It has been shown that high-quality (Fe/MgO) epitaxial heterostructures can be grown on both insulating (MgO) and semiconductor (GaAs and Si) substrates. The growth temperature determines the crystallinity of the Fe films and, more importantly, the morphology, with a transition from continuous to island-like growth modes for deposition temperatures between RT and 700 °C.

Magnetic characteristics such as anisotropies and dipolar interactions have been described and correlated with the structure at the atomic, nanometric and micrometric level. For single-layer elements, the size and in-plane interactions determine the magnetization processes, while in Fe/MgO multilayers the 3D nature of the system also involves 3D couplings. The great potential of magneto-optical techniques to characterize such structures, due to its sensitivity and easy implementation, has been specially emphasized. This way, it has been shown how the morphology in epitaxial Fe(001) continuous thin films strongly modifies the magnetization reversal process. In the case of arrays of monocrystalline tiles of single Fe layers and Fe/MgO multilayers, lateral dimensions and separations, both in and out of plane, play a relevant role determining the collective magnetic response via inter-tile and intra-tile dipolar interactions.

Finally, the application of fully epitaxial transition metal–insulator heterostructures for the development of MTJs has been also described, mentioning recent results in the Fe/MgO/Fe system.

Acknowledgments

We gratefully acknowledge the collaboration of our co-workers J V Anguita, B Bescós, M Bowen, F Briones, J F Calleja, F Cebollada, A V Chernykh, C Contreras, A Cornet, V Cros, A Fert, D García, J M García, F J M González, F G Güell, H Hernando, A Hernando-Mañeru, M R Ibarra, I-V Malikov, J I Martín, J L Menéndez, G M Mikhailov, L Morellón, E Navarro, F Peiró, F Petroff and H M De Teresa. We also acknowledge financial support from the Spanish Commission of Science and Technology, Comunidad de Madrid and the Acciones Integradas Hispano Francesas program.

References

[1] Meservey R and Tedrow P M 1994 *Phys. Rev. Lett.* **4** 173
[2] Meservey R and Tedrow P M 1994 *Phys. Rep.* **238** 173–243
[3] LeClair P, Moodera J S and Meservey R 1994 *J. Appl. Phys.* **76** 6546
[4] Cebollada A, Farrow R F C and Toney 2002 *Magnetic Nanostructures* ed H S Nalwa (Stevenson Ranch, CA: American Scientific) p 93
[5] Viret M, Samson Y, Marty A, Ott F, Søndergård E, Klein O and Fermon C 2000 *Phys. Rev. Lett.* **85** 3962
[6] Ohno Y, Young D K, Beschoten B, Matsukura F, Ohno H and Awschalom D D 1999 *Nature* **402** 790
[7] Zhu H J, Ramsteiner M, Kostial H, Wassermeier M, Schonherr H P and Ploog K H 2001 *Phys. Rev. Lett.* **87** 016601
[8] Grünberg P, Schreiber R, Pang Y, Brodsky M B and Sowers H 1986 *Phys. Rev. Lett.* **57** 2442
[9] Baibich M, Broto J M, Fert A, Nguyen van Dau F, Petroff F, Etienne P, Creuzet G and Friederich A 1988 *Phys. Rev. Lett.* **61** 2472

[10] Parkin S S P, More N and Roche K P 1990 *Phys. Rev. Lett.* **64** 2304
[11] Weller D and Doerner M F 2000 *Annu. Rev. Mater. Sci.* **30** 611
[12] See for example http://www.almaden.ibm.com/sst/
[13] Tehrani S, Slaughter J M, Chen E, Durlam M, Shi J and DeHerrera M 1999 *IEEE Trans. Magn.* **35** 2814
[14] See for example http://www.atalink.co.uk/mira/html/p172.htm
[15] Prinz G A 1998 *Science* **282** 1660
[16] Wolf S A, Awschalom D D, Buhrman R A, Daughton J M, von Molnár S, Roukes M L, Chtchlkanova A Y and Treger D M 2001 *Science* **294** 1488
[17] Harp G R 1999 *Thin Films, Heteroepitaxial Systems* ed W K Liu and M B Santos (Singapore: World Scientific) p 117
[18] Dingle R, Wiegmann W and Henry C H 1974 *Phys. Rev. Lett.* **33** 827
[19] Ortega J E and Himpsel F J 1992 *Phys. Rev. Lett.* **69** 844
[20] Balcells L l, Tholance J L, Linderoth S, Barbara B and Tejada J 1992 *Z. Phys.* B **89** 209
[21] Carl A and Wassermann E F 2002 *Magnetic Nanostructures* ed H S Nalwa (Stevenson Ranch, CA: American Scientific) p 59
[22] Albrecht M, Rettner C T, Moser A, Best M E and Terris B 2002 *Appl. Phys. Lett.* **81** 2875
[23] Jullière M 1975 *Phys. Lett.* A **54** 225
[24] Moodera J S and Mathon G 1999 *J. Magn. Magn. Mater.* **200** 248
[25] Moodera J S, Nassar J and Mathon G 1999 *Annu. Rev. Mater. Sci.* **29** 381
[26] Gustavsson F, George J M, Etgens V H and Eddrief M 2001 *Phys. Rev.* B **64** 184422
[27] Schuller I K, Kim S and Leighton C 1999 *J. Magn. Magn. Mater.* **200** 571
[28] Zabel H 2000 *Phil. Mag.* **80** 293
[29] Grünberg P 2001 *J. Phys.: Condens. Matter* **13** 7691
[30] de Miguel J J and Miranda R 2002 *J. Phys.: Condens. Matter* **14** R1063
[31] Kanaji T, Asano K and Nagata S 1973 *Vacuum* **23** 55
[32] Kanaji T, Kagotani T and Nagata S 1976 *Thin Solid Films* **32** 217
[33] Urano T and Kanaji T 1988 *J. Phys. Soc. Japan* **57** 3043
[34] Li C and Freeman A J 1991 *Phys. Rev.* B **43** 780
[35] Liu C, Park Y and Bader S D 1992 *J. Magn. Magn. Mater.* **111** L225
[36] Mezey L Z and Giber J 1982 *Japan. J. Appl. Phys.* 1 **21** 1569
[37] Overbury S H, Bertrand P A and Somorjay G A 1975 *Chem. Rev.* **75** 547
[38] Tasker P W and Duffy D M 1984 *Surf. Sci.* **137** 91
[39] Ehrlich G and Hudda F G 1966 *J. Chem. Phys.* **44** 1039
[40] Ehrlich G 1993 *Phys. Rev. Lett.* **70** 41
[41] Schwoebel R L and Shipsey E J 1966 *J. Appl. Phys.* **37** 3682
[42] Schwoebel R L 1969 *J. Appl. Phys.* **40** 614
[43] Thürmer K, Koch R, Weber M and Rieder K H 1995 *Phys. Rev. Lett.* **75** 1767
[44] Lairson B M, Payne A P, Brennan S, Rensing N M, Daniels B J and Clemens B M 1995 *J. Appl. Phys.* **78** 4449
[45] Kalff M, Breeman M, Morgenstern M, Michely T and Comsa G 1997 *Appl. Phys. Lett.* **70** 182
[46] McIntyre P C, Maggionre C J and Nastasi M 1995 *J. Appl. Phys.* **77** 6201
[47] Martínez Boubeta C, Menéndez J L, Costa-Krämer J L, García J M, Anguita J V, Bescós B, Cebollada A, Briones F, Chernykh A V, Malikov I V and Mikhailov G M 2001 *Surf. Sci.* **482** 910
[48] Martínez Boubeta C, Navarro E, Cebollada A, Briones F, Peiró F and Cornet A 2001 *J. Cryst. Growth* **226** 223
[49] Oka H, Subagyo A, Sawamura M, Sueoka K and Mukasa K 2001 *Japan. J. Appl. Phys.* **40** 4334
[50] Lawler J F, Schad R, Jordan S and van Kempen H 1997 *J. Magn. Magn. Mater.* **165** 224
[51] Ressier L, Diaz J and Peyrade J P 1997 *Appl. Phys. Lett.* **70** 2195
[52] Snoeck E, Ressier L, Jaffres H, Peyrade J P and Schuhl A 1998 *J. Cryst. Growth* **187** 245
[53] Jordan S M, Schad R, Herrmann D J L, Lawler J F and van Kempen H 1998 *Phys. Rev.* B **58** 13132
[54] Moons R, Blässer S, Dekoster J, Vantomme A, de Wacher J and Langouche G 1998 *Thin Solid Films* **324** 129
[55] Jordan S M, Schad R, Lawler J F, Herrmann D J L and van Kempen H 1998 *J. Phys.: Condens. Matter* **10** L355
[56] Jordan S M, Lawler J F, Schad R and van Kempen H 1998 *J. Appl. Phys.* **84** 1499
[57] Subagyo A, Sueoka K and Mukasa K 1999 *IEEE Trans. Magn.* **35** 3037
[58] Fashold G, Pucci A and Rieder K H 2000 *Phys. Rev.* B **61** 8475
[59] Fashold G, Priebe A and Pucci A 2001 *Appl. Phys.* A **73** 39
[60] Ventrice C A Jr and Geisler H 1999 *Thin Films: Heteroepitaxial Systems* ed W K Liu and M B Santos (Singapore: World Scientific) p 167
[61] Chambers S A 2000 *Surf. Sci. Rep.* **39** 105

[62] Yadavalli S, Yang M H and Flynn C P 1990 *Phys. Rev.* B **41** 7961
[63] Wu M C, Corneille J S, Estrada C A, He J W and Goodman D W 1991 *Chem. Phys. Lett.* **182** 472
[64] Wu M C, Corneille J S, He J W, Cesar C A and Goodman D W 1992 *J. Vac. Sci. Technol.* A **10** 1467
[65] Corneille J S, He J W and Goodman 1994 *Surf. Sci.* **306** 269
[66] Gallager M C, Fyfield M S, Cowin J P and Joyce S A 1995 *Surf. Sci.* **339** L909
[67] Chambers S A, Tran T T, Hileman T A and Jurgens T A 1994 *Surf. Sci.* **320** L81
[68] Wollschläger J, Erdös D and Schröder K M 1998 *Surf. Sci.* **402** 272
[69] Altieri S, Tjeng L H and Sawatzky G A 2001 *Thin Solid Films* **400** 9
[70] Valeri S, Altieri S, di Bona A, Giovanardi C and Moia T S 2001 *Thin Solid Films* **400** 16
[71] Schintke S, Messerli S, Pivetta M, Patthey F, Libioulle L, Stengel M, de Vita A and Schneider W D 2001 *Phys. Rev. Lett.* **87** 276801
[72] Park Y, Fullerton E E and Bader S D 1995 *J. Vac. Sci. Technol.* A **13** 301
[73] Dynna M, Vassent J L, Marty A and Gilles B 1996 *J. Appl. Phys.* **80** 2650
[74] Vassent J L, Dynna M, Marty A, Gilles B and Patrat G 1996 *J. Appl. Phys.* **80** 5727
[75] Keavney D J, Fullerton E E and Bader S D 1997 *J. Appl. Phys.* **81** 795
[76] Bowen M, Cros V, Petroff F, Fert A, Martínez Boubeta C, Costa-Krämer J L, Anguita J V, Cebollada A, Briones F, de Teresa J M, Morellón L, Ibarra M R, Güell F, Peiró F and Cornet A 2001 *Appl. Phys. Lett.* **79** 1655
[77] Zavaliche F, Przybylski M, Wulfhekel W, Grabowski J, Scholz R and Kirschner J 2002 *Surf. Sci.* **507–510** 560
[78] Przybylski M, Grabowski J, Zavaliche F, Wulfhekel W, Scholz R and Kirschner J 2002 *J. Phys. D: Appl. Phys.* **35** 1821
[79] Martínez Boubeta C, Cebollada A, Calleja J F, Contreras C, Peiró F and Cornet A 2003 *J. Appl. Phys.* **93** 2126
[80] Wulfhekel W, Klaua M, Ullmann D, Zavaliche F, Kirschner J, Urban R, Monchesky T and Heinrich B 2001 *Appl. Phys. Lett.* **78** 509
[81] Klaua M, Ullmann D, Barthel J, Wulfhekel W, Kirschner J, Urban R, Monchesky T L, Enders A, Cochran J F and Heinrich B 2001 *Phys. Rev.* B **64** 134411
[82] Popova E, Faure-Vincent J, Tiusan C, Bellouard C, Fishcer H, Hehn M, Montaigne F, Alnot M, Andrieu S, Schuhl A, Snoeck E and da Costa V 2002 *Appl. Phys. Lett.* **81** 1035
[83] Faure-Vincent J, Tiusan C, Bellouard C, Popova E, Hehn M, Montaigne F and Schuhl A 2002 *Phys. Rev. Lett.* **89** 107206
[84] Martínez Boubeta C, de Teresa J M, Costa-Krämer J L, Anguita J V, Serrate D, Arnaudas J I, Ibarra M R, Cebollada A and Briones F 2003 *J. Appl. Phys.* submitted
[85] Johnson M T, Bloemen P J H, den Broeder F J A and de Vries J J 1996 *Rep. Prog. Phys.* **59** 1409
[86] Tsymbal E Y and Pettifor D G 1997 *J. Phys.: Condens. Matter* **9** L411
[87] Li C, Wu R, Freeman A J and Fu C L 1993 *Phys. Rev.* **48** 8317
[88] Tanaka I, Mizuno M, Nakajyo S and Adachi H 1998 *Acta Mater.* **46** 6511
[89] Meyerheim H L, Popescu R, Kirschner J, Jedrecy N, Sauvage-Simkin M, Heinrich B and Pinchaux R 2001 *Phys. Rev. Lett.* **87** 076102
[90] Meyerheim H L, Popescu R, Jedrecy N, Vedpathak M, Sauvage-Simkin M, Pinchaux R, Heinrich B and Kirschner J 2002 *Phys. Rev.* B **65** 144433
[91] Li C, Freeman A J, Jansen H J F and Fu C L 1990 *Phys. Rev.* B **42** 5433
[92] Freeman A J and Fu C L 1987 *J. Appl. Phys.* **61** 3356
[93] Li C, Freeman A J and Fu C L 1988 *J. Magn. Magn. Mater.* **75** 201
[94] Ohnishi S, Freeman A J and Weinert M 1983 *Phys. Rev.* B **28** 6741
[95] Huang Y Y, Liu C and Felcher G P 1993 *Phys. Rev.* B **47** 183
[96] Goryunov Y V, Khaliullin G G, Garifullin I A, Tagirov L R, Schreiber F, Bödeker P, Bröhl K, Morawe Ch, Mühge Th and Zabel H 1994 *J. Appl. Phys.* **76** 6096
[97] Goryunov Y V, Garif'yanov N N, Khaliullin G G, Garifullin I A, Tagirov L R, Schreiber F, Mühge Th and Zabel H 1995 *Phys. Rev.* B **52** 13450
[98] Fermin J R, Antonio A, de Aguiar F M, Biao L and Rezende S M 1999 *J. Appl. Phys.* **85** 7316
[99] Park Y, Fullerton E E and Bader S D 1995 *Appl. Phys. Lett.* **66** 2140
[100] Wolfe J H, Kawakami R K, Ling W L, Qui Z Q, Arias R and Mills D L 2001 *J. Magn. Magn. Mater.* **232** 36
[101] Durand O, Childress J R, Galtier P, Bisaro R and Schuhl A 1995 *J. Magn. Magn. Mater.* **145** 111
[102] Krebs J J, Jonker B T and Prinz G A 1987 *J. Appl. Phys.* **61** 2596
[103] Zölfl M, Brockmann M, Köhler M, Kreuzer S, Schweinböck T, Miethaner S, Bensch F and Bayreuther G 1997 *J. Magn. Magn. Mater.* **175** 16
[104] Brockmann M, Zölfl M, Miethaner S and Bayreuther G 1999 *J. Magn. Magn. Mater.* **198/199** 384
[105] Xu Y B, Freeland D J, Tselepi M and Bland J A C 2000 *J. Appl. Phys.* **87** 6110

[106] Reiger E, Reinwald E, Garreau G, Ernst M, Zölfl M, Bensch F, Bauer S, Preis H and Bayreuther G 2000 *J. Appl. Phys.* **87** 5923
[107] Lépine B, Lallaizon C, Ababou S, Guivarc'h A, Députier S, Filipe A, Nguyen Van Dau F, Schuhl A, Abel F and Cohen C 1999 *J. Cryst. Growth* **201/202** 702
[108] Albrecht M, Furubayashi T, Przybylski M, Korecki J and Grandmann U 1992 *J. Magn. Magn. Mater.* **111** 207
[109] Berger A, Linke U and Oepen H P 1992 *Phys. Rev. Lett.* **68** 839
[110] Chen J and Erskine J 1992 *Phys. Rev. Lett.* **68** 1212
[111] Wu Y Z, Won C and Qiu Z Q 2002 *Phys. Rev.* B **65** 184419
[112] Choi H J, Qiu Z Q, Pearson J, Jiang J S, Li D and Bader S D 1998 *Phys. Rev.* B **57** R12713
[113] Contreras C, Menéndez J L, Cebollada A and Calleja J F 1999 *Japan. J. Appl. Phys.* **38** 6699
[114] Costa-Krämer J L, Menéndez J L, Cebollada A, Briones F, García D and Hernando A 2000 *J. Magn. Magn. Mater.* **210** 341
[115] Calleja J F, Menéndez J L, Cebollada A and Contreras C 2001 *Japan. J. Appl. Phys.* **40** 6829
[116] Contreras M C, Calleja J F, Rivas M, Gutiérrez M O and Corrales J A 1997 *J. Magn. Magn. Mater.* **175** 64
[117] Nowak J 1992 *J. Appl. Phys.* **72** 1490
[118] Cebollada F, Hernando-Mañeru A, Hernando A, Martínez Boubeta C, Cebollada A and González F J M 2002 *Phys. Rev.* B **66** 174410
[119] Slonczewski J C 1989 *Phys. Rev.* B **10** 6995
[120] Erickson R P, Hathaway K B and Cullen J R 1993 *Phys. Rev.* B **47** 2626
[121] Bruno P 1995 *Phys. Rev.* B **52** 411
[122] Pomerantz M, Slonczewski J C and Spiller E 1987 *J. Appl. Phys.* **61** 3747
[123] Bobo J F, Kikuchi H, Redon O, Snoeck E, Piecuch M and White R L 1999 *Phys. Rev.* B **60** 4131
[124] van der Heijden P A A, Bloemen P J H, Metselaar J M, Wolf R M, Gaines J M, van Eemeren J T W M, van der Zaag P J and de Jonge W J M 1997 *Phys. Rev.* B **55** 11569
[125] Néel L 1962 *C. R. Hebd. Scé. Acad. Sci.* 2 **55** 1676
[126] McCartney M R, Dunin-Borkowski R E, Scheinfein M R, Smith D J, Gider S and Parkin S S P 1999 *Science* **286** 1337
[127] Platt C L, McCartney M R, Parker F T and Berkowitz A E 2000 *Phys. Rev.* B **61** 9633
[128] Hehn M, Lenoble O, Lacour D, Féry C, Piécuch M, Tiusan C and Ounadjela K 2000 *Phys. Rev.* B **61** 11643
[129] Hehn M, Lenoble O, Lacour D and Schuhl A 2000 *Phys. Rev.* B **62** 11344
[130] Lacour D, Hehn M, Lenoble O, Schuhl A, Tiusan C and Ounadjela K 2001 *J. Appl. Phys.* **89** 8006
[131] Cowburn R P and Welland M 2000 *Science* **287** 1466
[132] Carcia P F, Mwinhaldt A D and Suna A 1985 *Appl. Phys. Lett.* **47** 178
[133] See for example http://www.almaden.ibm.com/sst/html/leadership/g09.htm
[134] Martín J I, Nogués J, Liu K, Vicent J L and Schuller I K 2003 *J. Magn. Magn. Mater.* **256** 449
[135] Nalwa H S (ed) 2002 *Magnetic Nanostructures* (Stevenson Ranch, CA: American Scientific)
[136] Rai-Choudhury P (ed) 1997 *Handbook of Microlithography, Micromachining and Microfabrication (SPIE Press Monograph PM39 and IEE Materials and Devices S12)* (Bellingham, WA: SPIE Optical Engineering Press)
[137] Costa-Krämer J L, Martín J I, Menéndez J L, Cebollada A, Anguita J V, Briones F and Vicent J L 2000 *Appl. Phys. Lett.* **76** 3091
[138] Kim S G, Otani Y, Fukamichi K, Yuasa S, Nyvlt M and Katayama T 1999 *J. Magn. Magn. Mater.* **198/199** 200
[139] Yu J, Rüdiger U, Thomas L, Parkin S S P and Kent A D 1999 *J. Appl. Phys.* **85** 5501
[140] Thomas L, Parkin S S P, Yu J, Rüdiger U and Kent A D 2000 *Appl. Phys. Lett.* **76** 766
[141] Yu J, Rüdiger U, Kent A D, Thomas L and Parkin S S P 1999 *Phys. Rev.* B **60** 7352
[142] Rüdiger U, Yu J, Kent A D and Parkin S S P 1999 *J. Magn. Magn. Mater.* **198/199** 261
[143] Kent A D, Rüdiger U, Yu J, Thomas L and Parkin S S P 1999 *J. Appl. Phys.* **85** 5243
[144] Rüdiger U, Yu J, Kent A D and Parkin S S P 1998 *Appl. Phys. Lett.* **73** 1298
[145] Rüdiger U, Yu J, Zhang S, Kent A D and Parkin S S P 1998 *Phys. Rev. Lett.* **80** 5639
[146] Ahmad E, Bland J A C and Gu E 1998 *IEEE Trans. Magn.* **34** 1099
[147] Blundell S J, Shearwood C, Gester M, Baird M J, Bland J A C and Ahmed H 1994 *J. Magn. Magn. Mater.* **135** L17
[148] Ebels U, Adeyeye A O, Gester M, Cowburn R P, Daboo C and Bland J A C 1997 *Phys. Rev.* B **56** 5443
[149] Ahmad E, Lopez-Diaz L, Gu E and Bland J A C 2000 *J. Appl. Phys.* **88** 354
[150] Kent A D, Rüdiger U, Yu J, Zhang S, Levy P M, Zhong Y and Parkin S S P 1998 *IEEE Trans. Magn.* **34** 900
[151] Xu Y B, Hirohata A, Lopez-Díaz L, Leung H T, Tselepi M, Garcdiner S M, Lee W Y, Bland J A C, Rousseaux F, Cambril E and Launois H 2000 *J. Appl. Phys.* **87** 7019
[152] Ebels U, Adeyeye A O, Gester M, Daboo C, Cowburn R P and Bland J A C 1997 *J. Appl. Phys.* **81** 4724

[153] Hanson M, Johansson C, Nilsson B, Isberg P and Wäppling R 1999 *J. Appl. Phys.* **85** 2793
[154] Fruchart O, Nozières J P, Wernsdorfer W and Givord D 1999 *Phys. Rev. Lett.* **82** 1305
[155] Jordan S M, Schad R, Keen A M, Bischoff M, Schmool D S and van Kempen H 1999 *Phys. Rev.* B **59** 7350
[156] Zölf M, Kreuzer S, Weiss D and Bayreuther G 2000 *J. Appl. Phys.* **87** 7016
[157] Armelles G, Costa-Krämer J L, Martín J I, Anguita J V and Vicent J L 2000 *Appl. Phys. Lett.* **77** 2039
[158] Martín J I, Vicent J L, Costa-Krämer J L, Menendez J L, Cebollada A, Anguita J V and Briones F 2000 *IEEE Trans. Magn.* **36** 3002
[159] Jaque D, Armelles G, Martín J I, Costa-Krämer J L, Briones F and Vicent J L 2002 *J. Magn. Magn. Mater.* **240** 37
[160] Martín J I, Costa-Krämer J L, Menéndez J L, Cebollada A, Anguita J V, Briones F and Vicent J L 2001 *J. Magn. Magn. Mater.* **226–230** 1875
[161] Jaque D, Martín J I, Armelles G, Costa-Krämer J L, Briones F and Vicent J L 2002 *J. Appl. Phys.* **91** 382
[162] Kim S G, Otani Y, Fukamichi K, Yuasa S, Nyvlt M and Katayama T 1999 *IEEE Trans. Magn.* **35** 2862
[163] Kohda T, Otani Y, Novosad V, Fukamichi K, Yuasa S, Nyvlt M and Katayama T 1999 *IEEE Trans. Magn.* **35** 3472
[164] Rüdiger U, Yu J, Thomas L, Parkin S S P and Kent A D 1999 *Phys. Rev.* B **59** 11914
[165] Demand M, Hehn M, Ounadjela K, Stamps R L, Cambril E, Cornette A and Rousseauz F 2000 *J. Appl. Phys.* **87** 5111
[166] Silva S L, Jenkins C R, York S M and Leibsle F M 2000 *Appl. Phys. Lett.* **76** 1128
[167] Kazakova O, Hanson M, Blomquist P and Wäppling R 2001 *J. Appl. Phys.* **90** 2440
[168] Hanson M, Johansson C, Nilsson B and Svedberg E B 2001 *J. Magn. Magn. Mater.* **246** 139
[169] Lauhoff G, Lee J, Bland J A C, Langridge S and Penfold J 1999 *J. Magn. Magn. Mater.* **198/199** 331
[170] Costa-Krämer J L, Anguita J V, Martín J I, Martínez Boubeta C, Cebollada A and Briones F 2002 *Nanotechnology* **13** 695
[171] Stamps R L and Camley R E 1999 *Phys. Rev.* B **60** 11694
[172] Schmitte T, Westerholt K and Zabel H 2002 *J. Appl. Phys.* **92** 4524
[173] Armelles G, Costa-Krämer J L, Martin J I, Anguita J V and Vicent J L 2000 *Appl. Phys. Lett.* **77** 2039
[174] García-Mochales P, Costa-Krämer J L, Armelles G, Briones F, Jaque D, Martín J I and Vicent J L 2002 *Appl. Phys. Lett.* **81** 3206
[175] Zak J, Moog E R, Liu C and Bader S D 1990 *J. Magn. Magn. Mater.* **89** 107
[176] Zak J, Moog E R, Liu C and Bader S D 1991 *Phys. Rev.* B **43** 6423
[177] Hund F 1927 *Z. Phys.* **40** 742
[178] Fowler R H and Nordheim L 1928 *Proc. R. Soc.* **119** 173–81
[179] Esaki L 1958 *Phys. Rev.* **109** 603–4
[180] Fisher J C and Giaver I 1961 *J. Appl. Phys.* **32** 172
[181] Simmons J G 1963 *J. Appl. Phys.* **34** 1793
[182] Brinkman W F, Dynes R C and Rowell J M 1976 *J. Appl. Phys.* **41** 1915
[183] Zeller H R and Giaver I 1969 *Phys. Rev.* **181** 789
[184] Sharma M, Wang S X and Nickel J H 1999 *Phys. Rev. Lett.* **82** 616
[185] de Teresa J M, Barthélémy A, Fert A, Contour J P, Lyonnet R, Montaigne F, Seneor P and Vaurès A 1999 *Phys. Rev. Lett.* **82** 4288
[186] Maekawa S and Gäfvert D 1982 *IEEE Trans. Magn.* **18** 707
[187] Suezawa Y and Gondo Y 1987 *Proc. Int. Symp. on Physics of Magnetic Materials (Sendai)* (Singapore: World Scientific) p 303
[188] Kabani R, Moodera J S, Tedrow P M and Meservey R 1990 *Mater. Res. Soc. Symp. Proc.* (Pittsburg, PA: Materials Research Society) p 117
[189] Nowak J and Rauluszkiewicz J 1992 *J. Magn. Magn. Mater.* **109** 79
[190] Schrag B D, Anguelouch A, Ingvarsson S, Xiao G, Lu Y, Trouilloud P L, Gupta A, Wanner R A, Gallagher W J, Rice P M and Parkin S S P 2000 *Appl. Phys. Lett.* **77** 2373
[191] Tegen S, Mönch I, Schumann J, Vinzelberg H and Schneider C M 2001 *J. Appl. Phys.* **89** 8169
[192] Miyazaki T and Tezuka T 1995 *J. Magn. Magn. Mater.* **139** L231
[193] Moodera J S, Kinder L R, Wong T M and Meservey R 1995 *Phys. Rev. Lett.* **74** 3273
[194] Luo Y and Samwer K 2001 *J. Appl. Phys.* **89** 6760
[195] Nowak J and Rauluszkiewicz J 1992 *J. Magn. Magn. Mater.* **109** 79
[196] Platt C L, Dieny B and Berkowitz A E 1997 *J. Appl. Phys.* **81** 5523
[197] Tsunoda M, Nishikawa K, Ogata S and Takahashi M 2002 *Appl. Phys. Lett.* **80** 3135
[198] Smith D J, McCartney M R, Platt C L and Berkowitz A E 1998 *J. Appl. Phys.* **83** 5154
[199] Gupta A, Li X W and Xiao G 2001 *Appl. Phys. Lett.* **78** 1894

[200] Lukaszew R A, Sheng Y, Uher C and Clarke R 1999 *Appl. Phys. Lett.* **75** 1941
[201] Sharma M, Nickel J H, Anthony T C and Wang S X 2000 *Appl. Phys. Lett.* **77** 2219
[202] Rottländer P, Kohlstedt H, Grünberg P and Girgis E 2000 *J. Appl. Phys.* **87** 6067
[203] Li Z, de Groot C and Moodera J H 2000 *Appl. Phys. Lett.* **77** 3630
[204] Rottländer P, Hehn M, Lenoble O and Schuhl A 2001 *Appl. Phys. Lett.* **78** 3274
[205] Lu Y, Li X W, Gong G Q, Xiao G, Gupta A, Lecoeur P, Sun J Z, Wang Y Y and Dravid V P 1996 *Phys. Rev.* B **54** R8357
[206] Obata T, Manako T, Shimakawa Y and Kubo Y 1999 *Appl. Phys. Lett.* **74** 290
[207] Jo M H, Mathur N D and Blamire M G 2002 *Appl. Phys. Lett.* **80** 2722
[208] O'Donnell J, Andrus A E, Oh S, Colla E V and Eckstein J N 2000 *Appl. Phys. Lett.* **76** 1914
[209] Tanaka M and Higo Y 2001 *Phys. Rev. Lett.* **87** 026602
[210] Sugahara S and Tanaka M 2002 *Appl. Phys. Lett.* **80** 1969
[211] Guth M, Dinia A, Schmerber G and van den Berg H A M 2001 *Appl. Phys. Lett.* **78** 3487
[212] Mathon J and Umerski A 1999 *Phys. Rev.* B **60** 1117
[213] Mathon J 2002 *J. Phys. D: Appl. Phys.* **35** 2437
[214] Oleinik I I, Tsymbal E Y and Pettiford D G 2000 *Phys. Rev.* B **62** 3952
[215] Oleinik I I, Tsymbal E Y and Pettiford D G 2001 *Phys. Rev.* B **65** 020401(R)
[216] MacLaren J M, Zhang X G and Butler W H 1997 *Phys. Rev.* B **56** 11827
[217] MacLaren J M, Butler W H and Zhang X G 1998 *J. Appl. Phys.* **83** 6521
[218] Mavropoulos Ph, Papanikolaou N and Dederichs P H 2000 *Phys. Rev. Lett.* **85** 1088
[219] Butler W H, Zhang X G, Schulthess T C and MacLaren J M 2001 *Phys. Rev.* B **63** 054416
[220] Mathon J and Umerski A 2001 *Phys. Rev.* B **63** 220403(R)
[221] Tsymbal E Y and Pettifor D G 2001 *Phys. Rev.* B **64** 212401(R)
[222] Uiberacker C and Levy P M 2001 *Phys. Rev.* B **64** 193404
[223] Zhang X G and Butler W H 2002 *APS March Meeting* p L15-2
[224] Wortmann D, Ishida H and Blügel S *TNT2002* p 185
[225] Jonker B T, Glembocki O J, Holm R T and Wagner R J 1997 *Phys. Rev. Lett.* **79** 4886
[226] Shoji A, Aoyagi M, Kosaka S, Shinoki F and Hayakawa H 1985 *Appl. Phys. Lett.* **46** 1098
[227] Talvacchio J, Gavaler J R, Braginski A I and Janocko M A 1985 *J. Appl. Phys.* **58** 4638
[228] Talvacchio J and Braginski A I 1987 *IEEE Trans. Magn.* **23** 859
[229] Kawakami A, Wang Z and Miki S 2001 *J. Appl. Phys.* **90** 4796
[230] Mijatovic D, Brinkman A, Oomen I, Rijnders G, Hilgenkamp H, Rogalla H and Blank D H A 2002 *Appl. Phys. Lett.* **80** 2141
[231] Lee W H, Cho H L, Cho B S, Kim J Y, Nam W J, Kim Y S, Jung W G, Kwon H, Lee J H, Lee J G, Reucroft P J, Lee C M and Lee E G 2000 *Appl. Phys. Lett.* **77** 2192
[232] Rabson D A, Jonsson-Akerman B J, Romero A H, Escudero R, Leighton C, Kim S and Schuller I K 2001 *J. Appl. Phys.* **89** 2786
[233] Moodera J S and Kinder L R 1996 *J. Appl. Phys.* **79** 4724
[234] Kiyomura T, Maruo Y and Gomi M 2000 *J. Appl. Phys.* **88** 4768
[235] Monsma D J and Parkin S S P 2000 *Appl. Phys. Lett.* **77** 720
[236] Yuasa S, Sato T, Tamura E, Suzuki Y and Yamamori H 2000 *Europhys. Lett.* **52** 344
[237] Mitani S, Moriyama T and Takanashi T 2002 *J. Appl. Phys.* **91** 7200
[238] Cabrera G G and García N 2002 *Appl. Phys. Lett.* **80** 1782
[239] Tsymbal E Y and Pettifor D G 1998 *Phys. Rev.* B **58** 432
[240] Itoh H, Shibata A, Kumazaki T, Inoue J and Maekawa S 1999 *J. Phys. Soc. Japan* **68** 1632
[241] Palasantzas G, Barnas J and de Hosson Th M 2000 *J. Appl. Phys.* **88** 927
[242] Montaigne F, Hehn M and Schuhl A 2001 *Phys. Rev.* B **64** 144402
[243] Tsymbal E Y, Mryasov O N and LeClair P 2003 *J. Phys.: Condens. Matter* **15** R109
[244] Jansen R and Lodder J C 2000 *Phys. Rev.* B **61** 5860
[245] Yuasa S, Nagahama T and Suzuki Y 2002 *Science* **297** 234